

# Local and global SAR constrained large tip angle 3D $k_T$ -points parallel transmit pulse design at 7 T

by

Filiz Yetişir

B.S., Electrical and Electronics Engineering

Bilkent University, 2011

Submitted to the Department of Electrical Engineering and Computer Science

in Partial Fulfillment of the Requirements for the Degree of

Master of Science in Electrical Engineering and Computer Science

at the

MASSACHUSETTS INSTITUTE OF TECHNOLOGY

February 2014

© 2014 Massachusetts Institute of Technology

All rights reserved.

Author .....  
Department of Electrical Engineering and Computer Science  
January 31, 2014

Certified by .....  
Elfar Adalsteinsson  
Associate Professor of Electrical Engineering and Computer  
Science; Harvard-MIT Division of Health Science and Technology  
Institute of Medical Engineering and Science  
Thesis Supervisor

Accepted by .....  
Leslie A. Kolodziejski  
Chairman, Department Committee on Graduate Students



# Local and global SAR constrained large tip angle 3D $k_T$ -points parallel transmit pulse design at 7 T

by

Filiz Yetişir

Submitted to the Department of Electrical Engineering and Computer Science

on January 31, 2014 in partial fulfillment of the

requirements for the degree of

Master of Science in Electrical Engineering and Computer Science

## Abstract

In the last decade, there has been a push towards higher main field strengths in magnetic resonance imaging (MRI) to achieve better contrast and higher signal to noise ratio (SNR). A drawback to current imaging systems at high field is transmit magnetic field inhomogeneity, which degrades both SNR and contrast. This inhomogeneity can be mitigated through radio frequency (RF) pulse design with conventional single-channel RF systems, but at the cost of impractically long pulses. Parallel transmit (pTx) systems with multiple independent and simultaneous RF transmit channels achieve transmit field inhomogeneity mitigation with practical pulse duration, but with potentially higher deposition of RF energy as measured by the specific absorption rate (SAR). In addition, RF pulse design becomes a more challenging task with pTx systems. The electric fields of independent channels can constructively interfere (linearly add up) at points in the body and create local hot spots, whose effect is quantified by local SAR. The peak local SAR inside the body needs to be kept under specified safety limits, hence a large number of constraints are forced upon the RF pulse during the design process. In order to avoid a large number of constraints which complicate and slow down the pulse design, it is possible to limit local SAR indirectly by limiting the RF pulse power. Although this approach results in a simplified and faster RF pulse design process, it is not optimal because pulse power and local SAR are not linearly related. At small tip angles (low RF energy deposition) with spokes trajectory, it has been demonstrated that the control of pulse power does not explicitly control local SAR and simultaneous constraints of pulse power and local SAR are required to yield optimal pulses satisfying system and regulatory limits. At large tip angles (high RF energy deposition) the local SAR constraint is more restricting for RF pulse performance relative to the small tip angle case. Therefore, the ability to design optimal RF pulses for the same constraints becomes more crucial at large tip angle regime. To our best knowledge, none of the existing large tip angle pTx pulse design methods are capable of controlling local SAR directly. In this thesis the

small tip angle approach is extended to large tip angle and local SAR, global SAR and pulse power constraints are explicitly incorporated in the design of 3D  $k_T$ -point large tip angle RF excitation pulses at 7 Tesla. It is demonstrated that the excitation fidelity of the large tip angle pulses improves significantly when local SAR constraint is imposed directly instead of indirectly via control of the peak RF power.

Thesis Supervisor: Elfar Adalsteinsson

Title: Associate Professor of Electrical Engineering and Computer Science; Harvard-MIT Division of Health Science and Technology; Institute of Medical Engineering and Science

# Acknowledgements

First, I would like to express my gratitude to my advisor Elfar Adalsteinsson. I am grateful to him for leading me towards becoming a self-disciplinary and independent researcher, for being so patient and caring in improving my skills, supporting and motivating me whenever I need and being an absolutely fantastic role model to me. I feel very lucky for working with him and going through the MIT experience in his guidance.

I would also want to thank Bastien Guerin whom I had the privilege to collaborate with throughout the last two years. I am grateful to him for conveying his precious insight on RF pulse design, planting the seeds of the work in this thesis and helping to develop it through valuable discussion sessions.

This work would not be possible without a happy lab environment. I especially thank Audrey Fan as her mentoring, sincere support, non-stop energy and enthusiasm made every moment I spent with her splendid and motivating. I also want to thank Trina Kok, Obaidah Abubashem, Borjan Gagoski, Itthi Chatnuntawech, Jeffrey Stout and Tarek Lahlou for their friendship as well as valuable discussions on many subjects. I am also thankful to Leslie Kolodziejski for sparing some of her valuable time to give me great advice and support.

I would like to thank my friends for contributing to my life and indirectly to this piece of work in various dimensions. I feel especially thankful to my dear friends Ozge Ozel and Ozge Karanfil Yigit. Their warm friendship, and sensibility as well as the unbelievable resemblance of our perspective of life and feelings have always made my time with them extremely joyful. I would also like to thank my friends Sukru Cinar, Bilge Zeren Aksu, Yildiz Sinangil, Burak Dura, Wardah Inam, Rohit Singh for making my life in MIT colorful and diverse. I thank Sultan Isik, my friend in Turkey for cheering me up from so far away with a skype call, a text message or with a birthday gift.

I feel truly grateful for having Oguzhan Uyar in my life who has been able to make my life much more beautiful in a very short amount of time. He set a great example for me with his originality and determination. Most importantly, his love and support has been a true source of happiness to me.

I cannot think of a way to express my gratitude to my family in words. My mom Nebahat, my dad Ramazan and my brother Ersin are the greatest gifts of life to me. I thank them for feeling my stress, excitement, happiness and pain at least as strongly as I do in their hearts both during my experience at MIT and throughout my whole life. Their unconditional love and care is an invaluable blessing to me.

Massachusetts Institute of Technology  
January 31, 2014

Filiz Yetişir



# Contents

1	Introduction .....	15
2	Background and Motivation .....	18
2.1	Origin of the MRI Signal .....	18
2.2	Excitation RF Pulse Design .....	21
2.3	Bloch Equations.....	22
2.4	Small Tip Angle (STA) Approximation .....	23
2.5	Specific Absorption Rate (SAR) .....	24
2.6	Parallel Transmission (pTx) .....	25
2.7	Excitation k-space Trajectory .....	26
2.8	Large Tip Angle (LTA) Pulse Design .....	27
3	Methods.....	28
3.1	LCLTA Method.....	28
3.2	Full Bloch Simulation Method.....	30
3.3	Simulation Data.....	35
3.4	Error Metrics .....	36
4	Results.....	38
4.1	Pulse Design .....	38
4.1.1	Pulse Design at Small Tip Angle .....	38
4.1.2	Small Tip Angle Pulse Design vs Large Tip Angle Pulse Design .....	40
4.1.3	Pulse Design at Large Tip Angle .....	44
4.2	Least Squares vs Magnitude Least Squares .....	47
4.3	Constrained Pulse Design.....	49
4.3.1	Effects of Constraints on Excitation Profile.....	49
4.3.2	L-Curves.....	50
5	Conclusion, Discussion and Future Work.....	62
6	References .....	65





# List of Figures

Figure 1: An atom with an odd number of protons or neutrons has magnetic properties similar to a small magnetic bar due to its charge & spin and an angular momentum due to its mass & spin. (Figure courtesy of M. J. Puddephat.) ..... 18

Figure 2: A precessing spin (an atom with an odd number of protons or neutrons) placed inside an external magnetic field. (Figure courtesy of M. J. Puddephat.) ..... 18

Figure 3: In the absence of  $B_0$  the spins are aligned randomly (left) whereas in the presence of  $B_0$  they (a fraction of them) are aligned with or against the direction of the field (right). (Figure courtesy of M. J. Puddephat.) ..... 19

Figure 4:  $B_1^+$  field tuned to the Larmor frequency of the targeted spins effectively tip the spins away from  $B_0$  towards the transverse plane. (Figure from (1) p. 25.)..... 20

Figure 5: Effect of  $B_1^+$  on spins in laboratory frame (top left) and in rotating frame (top right and bottom). (Figure courtesy of M. J. Puddephat.) ..... 20

Figure 6: The transverse component of magnetization induces a current in the receiver coils while the spin is returning back to its equilibrium state. (Figure courtesy of M. J. Puddephat.) ..... 21

Figure 7: An example  $k_T$ -points k-space trajectory is shown on the left. The RF energy is emitted at red dots while the black arrows represent the tracing order. An example excitation pulse sequence corresponding to the trajectory given is shown on the right. The gradient is zero during the RF pulse (we do not move in k-space). When not transmitting RF energy, we move in transmit k-space by turning on the x, y and z gradients. .... 27

Figure 8: The axial, sagittal and coronal (from left to right) visualization of the simulation data set..... 35

Figure 9: The magnitude and phase profiles of the individual channels through a slice right above the sinus cavity..... 36

Figure 10: The comparison between circularly polarized birdcage mode, RF shimming (1  $k_T$ -point), 2  $k_T$ -points, 3  $k_T$ -points and 5  $k_T$ -points cases at small tip angle using the small tip angle approximation method introduced in the Background section with a least squares algorithm. Target tip angle:  $10^\circ$  (target magnetization: 0.17), target phase: flat  $0^\circ$ . .... 39

Figure 11: The mean and the standard deviations of the magnetizations of the target, STA approximation model ( $A*b$  in Equation (2.15)) and the Bloch simulation for tip angles between  $10^\circ$  and  $90^\circ$ . A least squares algorithm was used with 1  $k_T$ -point. Target phase: flat  $0^\circ$ , volume of interest: a slice of thickness 4 mm, RF pulse duration: 0.5 ms. Perfectly homogenous  $B_1^+$  maps were used..... 41

Figure 12: The mean and the standard deviations of the magnetizations of the target and the Bloch simulation for the LCLTA design for target tip angles between  $10^\circ$  and  $180^\circ$ . A least squares algorithm was used with 1  $k_T$ -point. The target phase: flat  $0^\circ$ , volume of interest: a slice of thickness 4 mm, RF pulse duration: 0.5 ms. Perfectly homogenous  $B_1^+$  maps were used..... 42

Figure 13: The mean and the standard deviations of the magnetizations of the target and the Bloch simulation of the LCLTA design for target tip angles between 10° and 180°. A least squares algorithm was used with 9  $k_T$ -points. The target phase: flat 0°, volume of interest: a slice of thickness 4 mm, RF pulse duration 5.29 ms. Realistic  $B_1^+$  maps were used. .... 43

Figure 14: The mean and the standard deviations of the magnetizations of the target and the Bloch simulation for the full Bloch simulation design for target tip angles between 10° and 180°. A least squares algorithm was used with 9  $k_T$ -points. The target phase: 0°, volume of interest: a slice of thickness 4 mm, RF pulse duration 5.29 ms. Realistic  $B_1^+$  maps were used. .... 44

Figure 15: The comparison between circularly polarized birdcage mode, RF shimming (1  $k_T$ -point), 3  $k_T$ -points, 6  $k_T$ -points and 9  $k_T$ -points cases at large tip angle using the full Bloch simulation method with a least squares algorithm. Target tip angle: 90° (target magnetization: 1), target phase: flat 0°. .... 45

Figure 16: The comparison between circularly polarized birdcage mode, RF shimming (1  $k_T$ -point), 3  $k_T$ -points, 6  $k_T$ -points and 9  $k_T$ -points cases at large tip angle using the full Bloch simulation method with a least squares algorithm. Target tip angle: 180° (target magnetization: 1), target phase: flat 0°. .... 46

Figure 17: The comparison of the least squares (LS), magnitude least squares (MLS) and the least squares algorithm with the BC mode phase target (BC phase) for 1 and 2  $k_T$ -points. Target flip angle: 10°, target phase: flat 0° for LS and MLS, volume of interest: a slice of thickness 4mm. .... 47

Figure 18: The comparison of the least squares (LS), magnitude least squares (MLS) and the least squares algorithm with the BC mode phase target (BC phase) for 1 and 2  $k_T$ -points. Target flip angle: 90°, target phase: flat 0° for LS and MLS, volume of interest: a slice of thickness 4mm. .... 48

Figure 19: Comparison of the performances of an unconstrained RF pulse and a constrained RF pulse at small tip angle (20° target tip angle, 5  $k_T$ -points) and large tip angle (90° target tip angle, 5  $k_T$ -points) regimes. The constraint is a maximum RF voltage value of 30 V for both cases. .... 49

Figure 20: The comparison of peak 10g LSAR, GSAR and peak RF voltage constrained designs using 9  $k_T$ -points. Target tip angle: 90°, target phase: flat 0°. .... 50

Figure 21: The magnitude and phase of the resulting magnetization for all 16 slices of a point near the elbow of the LSAR constrained (blue) L-curve in Figure 20 with an RMMSE of 2 % and peak 10g LSAR of 1.2 W/kg. Design time: 60 s for LCLTA, 280 s for full Bloch simulation method. .... 51

Figure 22: Peak 10g LSAR, GSAR and peak RF voltage values of the three designs in Figure 20. .... 52

Figure 23: The comparison of peak 10g LSAR, GSAR and peak RF voltage constrained designs using 9  $k_T$ -points. Target tip angle: 90°, target phase: flat 0°. For all designs not exceeding the practical limits of 8 W/kg peak 10g LSAR, 3 W/kg GSAR and 200 V peak RF voltage was ensured. .... 52

Figure 24: Comparison of the 10g LSAR, GSAR and peak RF voltage values of the 3 curves (blue, green and red) in Figure 22 and Figure 23. .... 53

Figure 25: The comparison of peak 10g LSAR, GSAR and peak RF voltage constrained designs using 9  $k_T$ -points and a magnitude least squares algorithm. Target tip angle:  $90^\circ$ ..... 54

Figure 26: The comparison of peak 10g LSAR, GSAR and peak RF voltage constrained designs using 6  $k_T$ , 9  $k_T$  and 12  $k_T$  points with a least squares algorithm. Target tip angle:  $90^\circ$ , target phase:  $0^\circ$ ..... 55

Figure 27: Effect of down sampling the transmit field maps on the performance of LSAR, GSAR and RF constrained designs. Target tip angle:  $90^\circ$ , target phase: flat  $0^\circ$ , number of  $k_T$ -points: 9, algorithm: least squares..... 56

Figure 28: The comparison of the speed of the two algorithms with different down sampling rates for the transmit field maps for all three designs (LSAR, GSAR and RF constrained) in Figure 27..... 56

Figure 29: Effect of the tolerance value of the optimizing algorithm on the performance of LSAR, GSAR and RF constrained designs. Target tip angle:  $90^\circ$ , target phase: flat  $0^\circ$ , number of  $k_T$ -points: 9, algorithm: least squares..... 57

Figure 30: The comparison of the speed performance of the two algorithms with different tolerance values for the optimizing algorithm in Figure 29..... 58

Figure 31: The comparison of peak 10g LSAR, GSAR and RF peak voltage constrained inversion RF pulse designs using 9  $k_T$ -points and a least squares algorithm. Target tip angle:  $180^\circ$ ..... 59

Figure 32: The magnitude and phase of the resulting magnetization for all 16 slices of a point near the elbow of the LSAR constrained (blue) L-curve in Figure 31 with an RMMSE of 6 % and peak 10g LSAR of 2 W/kg. Design time: 47 s for LCLTA, 2131 s for full Bloch simulation method. .... 59

Figure 33: The comparison of peak 10g LSAR, GSAR and RF peak voltage constrained refocusing RF pulse designs using 12  $k_T$ -points and a least squares algorithm. Target tip angle:  $180^\circ$ , target phase: flat  $0^\circ$  (i.e. rotation axis for the spins: x-axis)..... 60

Figure 34: The magnitude and phase of the  $\beta$  (the target for the refocusing pulse design, Equation (3.26)) for all 16 slices of a point near the elbow of the LSAR constrained (blue) L-curve in Figure 33 with an RMMSE of 8 % and peak 10g LSAR of 2.5 W/kg. Design time: 76 s for LCLTA, 2080 s for full Bloch simulation method..... 61



# List of Tables

Table 1: The peak RF voltage, peak 10g local SAR and global SAR values of the pulses in Figure 10. A duty cycle of 10% was assumed..... 40

Table 2: The peak RF voltage, peak 10g local SAR and global SAR values of the pulses in Figure 15. A duty cycle of 10% was assumed..... 45

Table 3: The peak RF voltage, peak 10g local SAR and global SAR values of the pulses in Figure 16. A duty cycle of 10% was assumed..... 46



# 1 Introduction

Over the last few decades magnetic resonance imaging (MRI) has become a powerful and widespread imaging modality due to the extensive amount of information a magnetic resonance (MR) image provides about the structure and function of the human body. MRI is a flexible technique that can be applied to diagnosis of many diseases because it is sensitive to various tissue properties. Unlike some other commonly used imaging techniques such as X-ray and computer tomography, MRI has high soft tissue contrast as well as a non-invasive nature since it does not include ionizing radiation.

MRI makes use of the magnetic properties of various nuclei inside the body to form an image. Atoms with an odd number of protons and/or neutrons can be visualized as spinning charged spheres with a small magnetic moment. An MR scanner has three magnetic fields that interact with these spinning spheres -commonly called as spins- namely the main magnetic field ( $B_0$ ), the radio frequency (RF) field ( $B_1$ ) and the gradient field (G). In the absence of any magnetic field, these spins are randomly aligned and their net magnetic moment is zero. The main field causes some of the spins to align with it and hence have a net nonzero magnetic moment. Moreover, the spins exhibit resonance at a well-defined frequency called the Larmor frequency which depends on the main field strength, the atomic structure of the spin and the chemical environment in which the spin resides. If an RF field is applied at the Larmor frequency of some targeted spins, they are tipped away from their equilibrium state towards a plane perpendicular to the main field, called the transverse plane. After the RF field is removed, the spins exhibit precession at Larmor frequency around the main field and relax back to their equilibrium position, emitting an RF signal whose strength depend on the magnetic moment of the spins. This signal is then detected by specially designed RF coils and sent to a computer for image reconstruction. In summary, a typical MR experiment consists of two stages. First stage involves exciting the spins inside the body through the application of RF energy to create the MR signal and is termed 'excitation'. The second stage involves detecting the MR signal and reconstructing it to create an image and is termed 'acquisition'. Gradient fields that are usually linear in all three spatial dimensions are applied on top of the main field to obtain spatial selectivity during excitation and spatial encoding during acquisition (1). This thesis focuses on the excitation stage, in particular on the analysis and development of various methods of designing RF waveforms for high main magnetic field MRI systems.

In a typical MR application the targeted volume is either a thin slice (2D imaging) or a slab (3D imaging). Exciting only the targeted volume using spatially selective RF pulses is desirable because it results in shorter acquisition pulses and easier handling of the collected data. Furthermore, in specific applications spatially tailored pulses that excites not the whole slice but a special spatial pattern inside the slice could be advantageous. Moreover, it is important to keep the duration of the RF pulse as short as possible since the quality of the MR signal decays in time due to relaxation and main field inhomogeneities. Additionally, RF energy deposition to the body needs to be kept at minimum to avoid

excessive tissue heating. As a result, it is important to be able to design RF pulses that can achieve user-specific needs and enable the user to trade off different features of the excitation stage. For low main magnetic field strengths (below 3T), single slice and slab selective RF pulses are fairly simple to design.

In the last decade, there has been a push towards higher main magnetic field strengths to take advantage of higher signal to noise ratio (SNR) and improved image contrast. Nevertheless, some of the low field assumptions are no longer valid at high magnetic field strengths resulting in severely inhomogeneous RF transmit field distributions throughout the region of interest. For further discussion on the severe transmit field inhomogeneity at higher fields, see (2,3). As a consequence, the RF pulses needed to mitigate the RF field inhomogeneity at high field systems are impractically long. To overcome this issue, parallel transmission (pTx) technology has been proposed where multiple RF channels can transmit independent RF signals simultaneously. pTx does not only enable shorter RF pulses but it also gives the user extra degrees of freedom e.g. in controlling the power deposition, at the expense of more sophisticated and expensive hardware as well as a more complicated pulse design procedure (4,5).

MR imaging is subject to various restrictions due to both hardware limitations and safety concerns. MRI is a safe imaging modality as long as certain conditions as suggested by regulatory authorities are met. Main safety concerns include the effects of a strong static magnetic field, tissue heating (as measured by specific absorption rate, SAR) due to excessive RF energy deposition, nerve stimulation due to rapid gradient field change and discomfort and damage due to acoustic noise (6). The main magnetic field strength and the rate of gradient field change (slew rate) are fixed for an MR scanner and their limits are enforced through the hardware. On the other hand, SAR and acoustic noise are sequence dependent and need to be taken into account when designing an RF pulse sequence. Reduction of acoustic noise through RF pulse design (7,8) has been previously studied and is not the focus of this thesis. In this thesis we focus on the more challenging and restrictive problem of controlling SAR by incorporating it into the RF pulse design process. SAR control is especially important for pTx systems because independent waveforms can be played out through different channels simultaneously hence the electric fields of the channels can interfere constructively, creating local hot spots. Therefore for a pTx system keeping tissue heating (or SAR) under safety limits is a more challenging problem than it is for a single channel system. On the other hand, simultaneous independent RF waveforms also result in more degrees of freedom to achieve the desired excitation profile, making it possible to design multiple pulses that have the same transmit field inhomogeneity mitigation performance and choose the one with the lower SAR (9). As a result, a pTx system complicates the RF pulse design process while also giving extra degrees of freedom to minimize SAR for the same excitation fidelity.

Explicitly SAR constrained RF pulse design has been studied in small tip angle regime where the spins are tipped away from their equilibrium states by a small amount (10). However, at large tip angle regime, where RF energy deposition is much higher and SAR is a more restrictive limitation, no SAR constrained design methods are available to our best knowledge. The current methods control SAR indirectly by putting limitations on the peak RF voltage of the RF pulse, either assuming worst case scenario (11) or experimentally finding a good parameter in a regularized optimization scheme (12).



In this thesis, a local and global SAR constrained RF excitation pulse design algorithm for large target tip angles is introduced. This is proposed in the context of mitigating the transmit field inhomogeneity inside a targeted volume in human brain with a high field pTx system. The SAR constrained design is compared with the traditional RF peak voltage constrained design to demonstrate that direct control of SAR results in more optimal pulses than indirect control via limits on RF peak voltage. The developed algorithm is analyzed across several design parameters.

## 2 Background and Motivation

### 2.1 Origin of the MRI Signal

To understand MRI, it is first necessary to understand proton nuclear magnetic resonance (NMR). Although hydrogen in many molecules exhibit proton NMR, the hydrogen atom ( $^1\text{H}$ ) in water is the most relevant for MRI due to the abundance of water in body. A proton can be thought of as a spinning (rotating around its own axis) charged sphere associated with a mass. The spin and charge of a proton create an effect similar to that of a small magnetic bar while the spin and the mass together result in an angular momentum. It is important to note that the charged sphere model is only a classical mechanics analogy of the quantum spin used to visualize what a spin is. Proton NMR at the atomic level can only be explained by quantum physics but at the voxel level, the magnetization is formed by the addition of so many voxels that the analysis can be carried out in a classical point of view. Only atoms with an odd number of protons or neutrons have nonzero spin thus only such atoms exhibit the NMR phenomenon. Specifically, a spin inside an external magnetic field will start precessing about the axis of the magnetic field (see Figure 1) eventually aligning with or against it. This is true for all spins only at the absolute zero temperature. At higher temperatures, there is a competition between the effect of the magnetic field and the random motion of the  $^1\text{H}$  nucleus. At room temperature and with fields on the order of 1-100T, this random motion is large so that only a small fraction of the  $^1\text{H}$  spins are aligned with the external magnetic field. To visualize precession of a spin one can think of a spinning gyroscope placed in earth's gravitational field. The precessional frequency, called the Larmor frequency, is

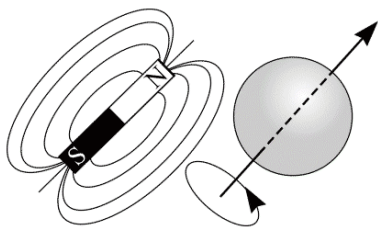


Figure 1: An atom with an odd number of protons or neutrons has magnetic properties similar to a small magnetic bar due to its charge & spin and an angular momentum due to its mass & spin. (Figure courtesy of M. J. Puddephat.)

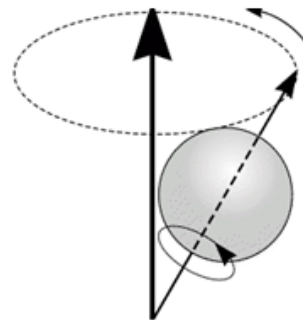


Figure 2: A precessing spin (an atom with an odd number of protons or neutrons) placed inside an external magnetic field. (Figure courtesy of M. J. Puddephat.)

determined by the strength of the external magnetic field as well as the characteristics of the atom. The proportionality constant between the Larmor frequency and the external magnetic field is called the gyromagnetic ratio ( $\gamma$ ) and it has units of  $rad/s/T$ . For  $^1H$ ,  $\gamma/2\pi = 42.58 MHz$ . (13)

The nature of MRI is based on the interaction of spins inside the body with three kinds of magnetic fields: main magnetic field ( $B_0$ ), radiofrequency field ( $B_1$ ) and gradient field ( $\vec{G} = [G_x G_y G_z]$ ). The main magnetic field is not varied during the MRI experiment and is usually a few Tesla. By convention the direction of  $B_0$  is called the longitudinal direction or the z-direction and the plane perpendicular to it is called the transverse plane or the x-y plane. The radiofrequency field lies on the transverse plane and is time varying. Its strength is usually a small fraction of a Gauss (1 Gauss =  $100\mu T$ ). The gradient field consists of three independent spatially varying components in x, y and z directions with field strengths on the order of a few Gauss/cm (1).

In the absence of  $B_0$  the spins (their angular momentum) orient randomly, such that their magnetic moments cancel and result in net zero macroscopic magnetic moment. Inside the main magnetic field  $B_0$  as mentioned earlier, the spins start precessing at their Larmor frequency and eventually a small fraction of them align either with or against the  $B_0$  direction. The equation governing the relation between  $B_0$  and the precessional frequency is called the Larmor Equation:

$$\omega_0 = \gamma B_0 \tag{2.1}$$

At room temperature, the number of spins aligning with the direction of  $B_0$  is slightly higher than the number of spins aligning against it. Hence a net macroscopic magnetic moment ( $M_0$ ) in the direction of the main magnetic field is created.

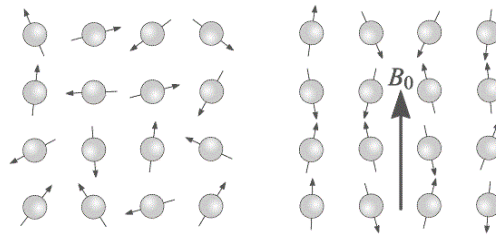


Figure 3: In the absence of  $B_0$  the spins are aligned randomly (left) whereas in the presence of  $B_0$  they (a fraction of them) are aligned with or against the direction of the field (right). (Figure courtesy of M. J. Puddephat.)

In order for spins to emit an NMR signal, they must first absorb radio frequency (RF) energy (i.e. be “excited”). An RF pulse is fed into transmitter RF coils to create the desired transmit field, or  $B_1^+$  field (as opposed to  $B_1^-$ , receive field), that will tip the spins away from their equilibrium states towards the transverse plane. The RF pulse must be tuned to the Larmor frequency of the targeted spins to be able to effectively tip them. (See Figure 4) In the laboratory frame, both the spins and the  $B_1^+$  field rotate around the main magnetic field. Mathematically, it is easier to describe the behavior of spins in a

rotating frame of reference that rotates, like the spins, at the Larmor frequency around the longitudinal axis ( $B_0$ ) (1). The effect of a constant  $B_1^+$  on the spins in the rotating frame can be visualized as in Figure 5. The angle between the magnetization of the spins and the longitudinal axis after the application of the RF pulse is called the tip angle and it depends on the duration and the magnitude of the RF pulse. After the RF pulse, an RF signal is induced in the receiver coil by the rotating transverse component of the magnetization because the “excited” spin releases the RF energy it absorbed previously (See Figure 6). In summary, a typical MR sequence has two stages. In the first stage, the spins are excited using RF energy and are tipped towards the transverse plane (excitation). In the second stage, the signal the spins emit when returning back to their equilibrium state is collected and stored for image reconstruction (acquisition). It is possible and desirable to control some parameters of the excitation and acquisition stages to image different properties of the human body. In this work, we will focus on designing RF pulses for the excitation stage.

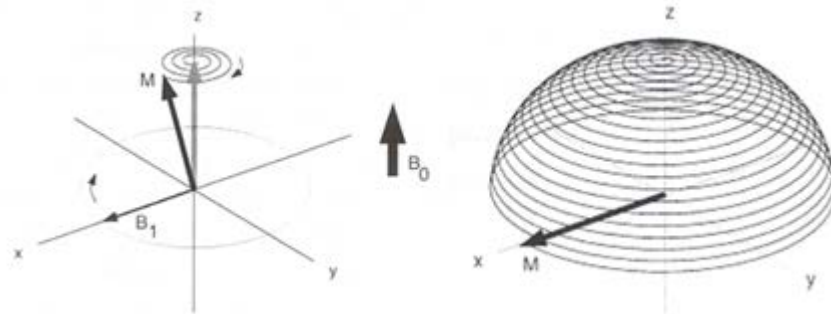


Figure 4:  $B_1^+$  field tuned to the Larmor frequency of the targeted spins effectively tip the spins away from  $B_0$  towards the transverse plane. (Figure from (1) p. 25.)

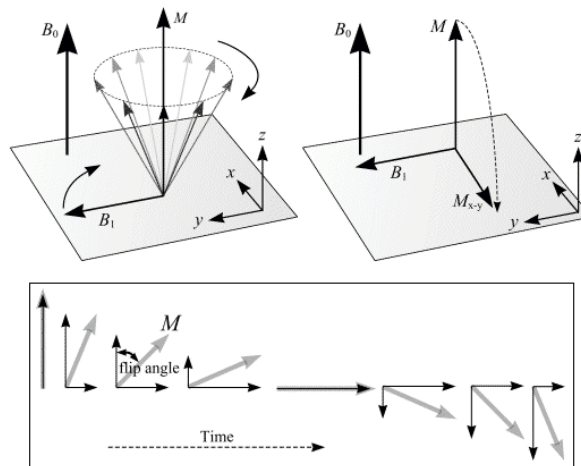


Figure 5: Effect of  $B_1^+$  on spins in laboratory frame (top left) and in rotating frame (top right and bottom). (Figure courtesy of M. J. Puddephat.)

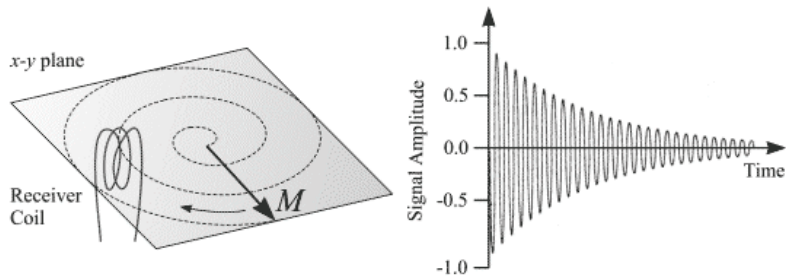


Figure 6: The transverse component of magnetization induces a current in the receiver coils while the spin is returning back to its equilibrium state. (Figure courtesy of M. J. Puddephat.)

## 2.2 Excitation RF Pulse Design

In excitation pulse design, it is crucial to have control over parameters such as the target excitation, pulse power and pulse duration. The target excitation could be a flat excitation over a thin slice (2D excitation) or a thick slab (3D excitation) as well as a specific shape on the transverse plane (spatially tailored excitation). In case of flat slice or slab excitation, the aim is to obtain a homogeneous excitation profile, i.e. the same flip angle at every point inside the slice or the slab. However, for main field strengths at or above 3T, homogenous excitation becomes a challenging task due to an effect called central brightening (2). This effect, which causes an excitation profile that is bright at the coil center and darker towards the peripheral instead of a flat one, occurs mostly due to constructive interference of the fields at different channels of the coil and wavelength effects (These effects occur because the wavelength of the RF signal becomes comparable with human body dimensions at high fields). The RF pulse and gradient fields can be used in combination to mitigate the  $B_1^+$  field inhomogeneities. Hence, a usual excitation pulse design includes designing four waveforms: RF,  $G_x$ ,  $G_y$  and  $G_z$ .

If there were no restrictions on the RF and gradient waveforms, it would be possible to obtain fairly good excitation fidelities depending on the encoding capabilities of the RF coil. Nevertheless, there are hardware, safety and practicality limitations on the waveforms that disrupt the resulting excitation fidelity. Hardware limitations on the waveform include the maximum output power of the RF power amplifiers (RFPAs), maximum gradient strength and the slew rate of the gradient coils. The maximum power output determines the maximum peak voltage of the RF waveform, whereas the maximum gradient strength and the slew rate determine the allowable peak value and maximum achievable slope of the gradient waveform. One of the most important safety limitations is the amount of RF energy deposition into the body which may cause tissue heating and possible cell death at high temperatures.

The RF energy deposition is quantified by the specific absorption rate (SAR) which is defined as the power absorbed per mass of tissue (units W/kg). Finally, the duration of an RF pulse should be short enough for several reasons including signal decay due to relaxation, the effect of imperfections such as main field inhomogeneities on the excitation fidelity and the scan time practicality. In conclusion, excitation pulse design is an essential part of an MR experiment which allows optimal excitation fidelities by ensuring that the system is used to its fullest potential while the limits are not exceeded.

## 2.3 Bloch Equations

Bloch Equations describe the behavior of the magnetization vector in a magnetic field. Ignoring relaxation, they can be expressed compactly as:

$$\frac{d\mathbf{M}}{dt} = \mathbf{M} \times \gamma \mathbf{B} \quad (2.2)$$

where

$$\mathbf{B} = \mathbf{B}_0 + (\mathbf{G} \cdot \mathbf{r})\mathbf{k} + \mathbf{B}_1^{lab} \quad (2.3)$$

and  $\mathbf{B}_1^{lab}$  refers to the RF field in laboratory frame. Assuming a circularly polarized RF field

$$\mathbf{B}_1^{lab} = B_1(t)[\mathbf{i} \cos(\omega \cdot t) - \mathbf{j} \sin(\omega t)] \quad (2.4)$$

Bloch Equation in matrix form becomes

$$\begin{pmatrix} \dot{M}_x \\ \dot{M}_y \\ \dot{M}_z \end{pmatrix} = \gamma \begin{pmatrix} 0 & B_z & -B_y \\ -B_z & 0 & B_x \\ B_y & -B_x & 0 \end{pmatrix} \begin{pmatrix} M_x \\ M_y \\ M_z \end{pmatrix} \quad (2.5)$$

where

$$B_z = B_0 + \mathbf{G} \cdot \mathbf{r} \quad (2.6)$$

$$B_x = B_{1,x}^{lab}, \quad B_y = B_{1,y}^{lab} \quad (2.7)$$

For simplicity we will work in the rotating frame of reference. It can be shown that (1) in the rotating frame, the form of the Bloch Equations is the same as their form in the laboratory frame

$$\frac{d\mathbf{M}^{rot}}{dt} = \mathbf{M}^{rot} \times \gamma \mathbf{B}^{rot} \quad (2.8)$$

In matrix form

$$\begin{pmatrix} \dot{M}_x^{rot} \\ \dot{M}_y^{rot} \\ \dot{M}_z^{rot} \end{pmatrix} = \gamma \begin{pmatrix} 0 & \mathbf{G} \cdot \mathbf{r} & -B_{1,y} \\ -\mathbf{G} \cdot \mathbf{r} & 0 & B_{1,x} \\ B_{1,y} & -B_{1,x} & 0 \end{pmatrix} \begin{pmatrix} M_x^{rot} \\ M_y^{rot} \\ M_z^{rot} \end{pmatrix} \quad (2.9)$$

As a result, the magnetization vector in the rotating frame can be visualized in a similar way to the magnetization vector in the laboratory frame i.e.  $\mathbf{M}^{rot}$  precesses around  $\mathbf{B}^{rot}$  with frequency  $\gamma|\mathbf{B}^{rot}|$  (similarly  $\mathbf{M}$  precesses around  $\mathbf{B}_z^{lab}$  with frequency  $\gamma|\mathbf{B}_z^{lab}|$ ). The solution of excitation is simplified this way because it is easier to visualize  $\mathbf{B}^{rot}$  than it is to visualize  $\mathbf{B}^{lab}$  (1).

## 2.4 Small Tip Angle (STA) Approximation

Although rotating frame of reference simplifies the Bloch Equations, finding an analytical expression of the temporal behavior of the magnetization vector for arbitrary excitatory RF and gradient fields is a challenging task because all three components of the magnetization are coupled. Small tip angle approximation further simplifies the Bloch Equations by assuming that the spins are tipped by a small amount so that the longitudinal component of the magnetization remains constant, i.e.  $M_z \approx M_0$ . Defining

$$M_{xy} = M_x^{rot} + iM_y^{rot} \quad (2.10)$$

$$B_1 = B_{1,x} + iB_{1,y} \quad (2.11)$$

The first two components of the Bloch Equation in matrix form can be written as

$$\dot{M}_{xy} = -i\gamma\mathbf{G} \cdot \mathbf{r}M_{xy} + i\gamma B_1 M_0 \quad (2.12)$$

Assuming that the system is initially in the state  $(0, 0, M_0)$  the solution of the differential equation is (14)

$$M_{xy}(\mathbf{r}) = i\gamma M_0 \int_0^T B_1(t) e^{-i\gamma\mathbf{r} \cdot \int_t^T \mathbf{G}(s) ds} dt \quad (2.13)$$

We define a spatial frequency variable

$$\mathbf{k}(t) = -\gamma \int_t^T \mathbf{G}(s) ds \quad (2.14)$$

We can see that  $\mathbf{k}(t)$  parametrically defines a path through the spatial frequency space. Hence in the small tip angle domain, we can view the transverse magnetization as the Fourier transform of the path  $\mathbf{k}(t)$  weighted by the RF pulse (14). The spatial frequency space is conventionally called the excitation k-space. Discretizing Equation (2.13), we obtain the following linear relation between the RF pulse and the resulting transverse magnetization:

$$\mathbf{m} = \mathbf{A}\mathbf{x} \quad (2.15)$$

$\mathbf{m}_{N \times 1}$  is the discretized transverse magnetization in the targeted volume,  $\mathbf{A}_{N \times M}$  is the system matrix representing the Fourier kernel  $e^{-i\gamma\mathbf{r} \cdot \mathbf{k}(t)}$  and the sensitivity of the coil inside the VOI and  $\mathbf{x}_{M \times 1}$  is the time discretized RF pulse (N: number of voxels, M: number of time points). Due to the fact that the

system matrix  $\mathbf{A}$  is usually a tall matrix (there are more voxels than discretized excitation points), a solution for  $\mathbf{x}$  can be found by a least squares optimization algorithm

$$\min_{\mathbf{x}} \|\mathbf{A}\mathbf{x} - \mathbf{m}_{target}\|_w^2 \quad (2.16)$$

where  $w$  refers to a weighting for the voxels. It is also possible to optimize only for the magnitude using a magnitude least squares approach (15). In that case Equation (2.16) can be modified in the following way:

$$\min_{\mathbf{x}} \||\mathbf{A}\mathbf{x}| - |\mathbf{m}_{target}|\|_w^2 \quad (2.17)$$

Nevertheless, unlike the least squares (LS) problem in Equation (2.16), the MLS problem is not convex, hence finding the global minimum is generally not guaranteed. One way of solving for the RF pulse in Equation (2.17) is to solve for the RF pulse iteratively in the following least squares problem:

$$\begin{aligned} \min_{\mathbf{x}_i} \||\mathbf{A}\mathbf{x}_i - \mathbf{z}_i|\mathbf{m}_{target}\|_w^2 \\ \text{s.t. } |\mathbf{z}_i| = 1 \end{aligned} \quad (2.18)$$

Where  $\mathbf{x}_i$  is the solution to the  $i$ th iteration.  $\mathbf{z}_i$  is updated with the phase of  $\mathbf{A}\mathbf{x}_i$  at every iteration. This way the phase constraint will be relaxed and one of the local minimum points of the MLS problem will be reached depending on the starting values for  $\mathbf{x}$  and  $\mathbf{z}$ .

## 2.5 Specific Absorption Rate (SAR)

It is possible to add the restrictions on an RF pulse into the minimization in Equation (2.16) and Equation (2.17). The peak amplitude and SAR are among the main constraints of an RF pulse. As mentioned before, specific absorption rate is a measure of the energy absorbed per mass of tissue. SAR is usually averaged over the whole body (global SAR, GSAR) or a small sample of volume, usually 1g or 10g of tissue (local SAR, LSAR). SAR at location  $\mathbf{r}$  can be calculated as follows

$$SAR(\mathbf{r}) = \frac{1}{T} \int_0^T \frac{\sigma(\mathbf{r})}{\rho(\mathbf{r})} |\mathbf{E}(\mathbf{r})|^2 dt \quad (2.19)$$

where  $\sigma(\mathbf{r})$  is the conductivity,  $\rho(\mathbf{r})$  is the density,  $\mathbf{E}(\mathbf{r})$  is the electric field at  $\mathbf{r}$  and  $T$  is the pulse duration.

$$\mathbf{E}(\mathbf{r}, t) = \mathbf{F}(\mathbf{r})\mathbf{b}(t) \quad (2.20)$$

with  $\mathbf{F}(\mathbf{r})$  representing the electric field sensitivities of different channels at location  $\mathbf{r}$ . Discretizing equation (2.19), we obtain

$$SAR(\mathbf{r}) = \frac{1}{M} \sum_{i=0}^M \mathbf{b}_i^H \left( \frac{\sigma(\mathbf{r})\mathbf{F}^H(\mathbf{r})\mathbf{F}(\mathbf{r})}{\rho(\mathbf{r})} \right) \mathbf{b}_i \quad (2.21)$$



where  $M$  is the number of time points. The term inside the parenthesis is called the SAR matrix at location  $\mathbf{r}$  and is independent of time. To calculate the 1g or 10g local SAR or the global SAR, the SAR matrices inside the corresponding volumes (a volume of mass 1g, 10g or the whole, respectively) are averaged. As a result the calculation of SAR matrices is independent from the pulse design procedure.

In order to satisfy LSAR limits at every voxel, one constraint for every voxel must be added into the optimization algorithm. However, a typical MR experiment has millions of body voxels leading to an unrealistically slow pulse design process. Even when the 10g average local SAR is calculated, the number of SAR matrices to consider is too high to have a practical algorithm. To overcome this issue, a concept called virtual observation points (VOPs) was proposed such that if the LSAR limits are satisfied for the VOPs (a few hundreds many) then it is guaranteed to satisfy the LSAR limits throughout the whole body with a predetermined overestimation factor (16). Then, the optimization algorithm in Equation (2.16) becomes the following constrained optimization (10):

$$\begin{aligned} & \min_{\mathbf{b}} \|\mathbf{A}\mathbf{b} - \mathbf{m}_{target}\|_w^2 && (2.22) \\ \text{subject to} & |b(j)| < b_{max} \quad \forall j \in \{1, \dots, M\} && \text{(RF peak amplitude constraint)} \\ & \frac{1}{M} \sum_{i=0}^M \mathbf{b}_i^H \mathbf{S}_v \mathbf{b}_i < LSAR_{max} \quad \forall v \in V && \text{(LSAR constraints)} \\ & \frac{1}{M} \sum_{i=0}^M \mathbf{b}_i^H \mathbf{S}_g \mathbf{b}_i < GSAR_{max} && \text{(GSAR constraint)} \end{aligned}$$

## 2.6 Parallel Transmission (pTx)

In the last decade, there has been a push towards higher main field strengths in order to have better contrast and higher signal to noise ratio (SNR). Nevertheless, as mentioned earlier, at higher field strengths the  $B_1$  field is no longer homogeneous inside the volume of interest because the wavelength of the RF signal becomes comparable with human body dimensions. To compensate the spatial variations in the transmit field, RF pulses with impractically long durations are needed. Furthermore, mitigating the  $B_1^+$  field inhomogeneities becomes very difficult using only the RF pulse without any gradients. The concept of parallel transmission was proposed in order to mitigate  $B_1$  field inhomogeneities with pulses of practical durations by playing independent RF waveforms on each channel of a transmit coil simultaneously (5). The extra degrees of freedom that pTx systems provide can effectively be utilized to accelerate the RF pulse. Recently, it has been shown that they can also be used to minimize the SAR. On the other hand, it is more complicated to manage SAR for a pTx system than a single channel system. With multiple independent transmission channels having electric fields with complex topology depending on the local tissue properties, SAR hot spots can occur at locations where the fields add up constructively. In particular, the proportionality relation between local SAR and global SAR that exists in single channel systems is lost in pTx systems (9). Hence, unlike the single channel case, it is no longer enough to track only the global SAR. Nevertheless, the advantages of having

practical pulses for  $B_1$  field inhomogeneity mitigation and spatially tailored excitation as well as minimizing SAR make the use of pTx desirable in spite of a more complicated pulse design process.

Equation (2.13) needs to be modified for pTx systems in the following way;

$$M_{xy}(\mathbf{r}) = i\gamma M_0 \sum_c S_c(\mathbf{r}) \int_0^T B_1(t) e^{-i\gamma \mathbf{r} \cdot \int_t^T \mathbf{G}(s) ds} dt \quad (2.23)$$

where  $S_c(\mathbf{r})$  refer to the sensitivity of channel  $c$  at location  $\mathbf{r}$ . Thus equation (2.15) becomes

$$\mathbf{m} = \mathbf{A}_{total} \mathbf{b}_{total} \quad (2.24)$$

$$\mathbf{A}_{total} = [\mathbf{A}_1 \quad \cdots \quad \mathbf{A}_C] \text{ and } \mathbf{b}_{total} = \begin{bmatrix} \mathbf{b}_1 \\ \vdots \\ \mathbf{b}_C \end{bmatrix} \quad (2.25)$$

where  $C$  is the number of transmit coil channels.

## 2.7 Excitation k-space Trajectory

To obtain a solution for the minimization in equation (2.16), the system matrix containing the RF field sensitivities and the k-space trajectory needs to be computed. The RF field sensitivities are hardware dependent thus cannot be controlled once the transmit coil is designed. On the other hand, the k-space trajectory is determined by the gradient pulses and therefore can be changed at will. Conventionally, a trajectory is decided on prior to the optimization of the RF pulse, hence the three gradient waveforms are predetermined. However, it is also possible to incorporate the choice of k-space trajectory in the optimization process at the cost of a slower and more complicated design procedure (17). In this thesis, we will predetermine the k-space trajectory and focus on 3D excitation using  $k_T$ -points (18). In this method, the RF energy is transmitted only at stationary points in k-space called the  $k_T$ -points (Figure 7).

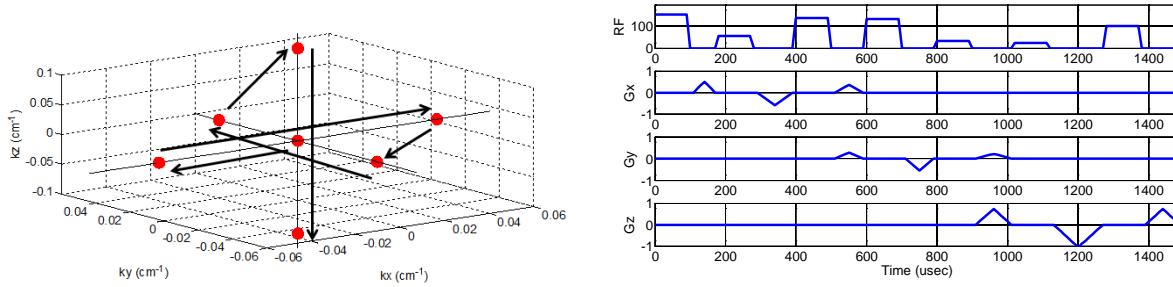


Figure 7: An example  $k_T$ -points k-space trajectory is shown on the left. The RF energy is emitted at red dots while the black arrows represent the tracing order. An example excitation pulse sequence corresponding to the trajectory given is shown on the right. The gradient is zero during the RF pulse (we do not move in k-space). When not transmitting RF energy, we move in transmit k-space by turning on the x, y and z gradients.

## 2.8 Large Tip Angle (LTA) Pulse Design

The linearized formulation in equation (2.22) works well for small tip angles. At larger tip angles, the nonlinearity of the Bloch equations becomes non-negligible and thus STA approximation performs poorly. There has been several suggested design approaches for large tip angle pulse design including linear class of large tip angle (LCLTA) pulses (19), Shinnar Le-Roux algorithm (20), Powell method (21), additive angle approach (22), optimal control approach (23) and composite pulses (24). Most of these methods result in pulses with reasonably well excitation fidelities at large tip angles. The LCLTA approach works well around  $90^\circ$  tip angle but fails drastically at  $180^\circ$  tip angle.

At high tip angles, more RF power is needed to tip the spins compared to the small tip angle case. As a result, the pulses designed are limited more severely by the SAR regulations. Hence, obtaining optimal pulses for a given SAR limit becomes especially important at high tip angles. To our best knowledge, none of the aforementioned methods have an explicit and direct SAR control incorporated in their pTx pulse design procedure. They either consider the worst case scenario where all electric fields are assumed to linearly add up (all electric fields in phase), control the RF peak and average power or use the VERSE method where a designed pulse is later adjusted to have below the limits SAR values. These approaches over-restrict the RF pulse in order to control SAR and therefore do not, in general, yield optimal excitation pulses with the best possible excitation fidelity consistent with the SAR regulatory limits.

In this work a SAR constrained large tip angle pulse design method to mitigate  $B_1^+$  field inhomogeneities at high field is developed.

## 3 Methods

As mentioned earlier, pulse design is nonlinear due to the Bloch equation but it is possible to linearize the Bloch equation for small target tip angles and obtain a simple Fourier transform based pulse design method (STA approximation). The analysis of why the STA approximation continues to work well beyond the small tip angle regime lead to the linear class of large tip angle (LCLTA) pulses, a class of large tip angle pulses that can be designed with a linear Fourier transform approach (19).

### 3.1 LCLTA Method

The LCLTA method is based on a generalization of the STA approximation. It can be constructed in three steps:

*Step 1:* Small-excitation approximation is a generalization of the STA approximation in the spinor domain. The STA approximation assumes that the initial magnetization is along +z direction and the tip angle between the initial and the final magnetizations is small, whereas small-excitation approximation makes no assumptions on the initial magnetization and the tip angle can be large. However, the effect of the RF waveform should be small.

*Step 2:* The small-excitation approximation is then applied to the special case of inherently refocused pulses. Inherently refocused pulses are Hermitian symmetric pulses (for every point in k-space there is a symmetric point with respect to the origin with the conjugate RF weighting) whose k-space trajectory starts at the origin. In the small-excitation regime an inherently refocused pulse produces a rotation around the axis of RF and the amount of rotation is approximately the Fourier transform of the RF-weighted k-space trajectory

$$\theta = \gamma \int_0^T B_1^*(t) e^{-ir \cdot k(t)} dt \quad (3.1)$$

where  $\theta$  is the flip angle.

*Step 3:* If the axis along which the RF waveform is applied stays the same, multiple small-excitation inherently refocused pulses can be concatenated to achieve higher flip angles and the final tip angle will simply be the sum of individual tip angles because rotations around the same axis add up linearly. Assume an RF pulse is decomposable into a sequence of K small-excitation inherently refocused sub-pulses and that the RF axis is stationary. Let the *i*th sub-pulse start at time  $T_{i-1}$  and end at time  $T_i$ . The rotation due to the *i*th sub-pulse is then

$$\theta_i = \gamma \int_{T_{i-1}}^{T_i} B_1^*(t) e^{-ir \cdot \mathbf{k}_i(t)} dt \quad (3.2)$$

where  $\mathbf{k}_i(t)$  is defined as

$$\mathbf{k}_i(t) = \gamma \int_t^{T_i} \mathbf{G}(s) ds \quad (3.3)$$

The resulting tip angle when all K sub-pulses are applied in order is:

$$\theta = \sum_{i=1}^K \theta_i \quad (3.4)$$

$$= \sum_{i=1}^K \gamma \int_{T_{i-1}}^{T_i} B_1^*(t) e^{-ir \cdot \mathbf{k}_i(t)} dt \quad (3.5)$$

$$= \gamma \int_0^T B_1^*(t) e^{-ir \cdot \mathbf{k}(t)} dt \quad (3.6)$$

The last equality follows because  $\mathbf{k}(t)$  is the concatenation of  $\mathbf{k}_i(t)$ s. Equation (3.6) means if a large tip angle pulse can be broken into inherently refocused small excitation pulses then it can be designed easily using a simple Fourier transform relation. Thus the same optimization algorithm that is used for the STA method in equation (2.16) can be used for the LCLTA method with the following modified objective function:

$$\boldsymbol{\theta} = \mathbf{A}_{LCLTA} \mathbf{x}^* \quad (3.7)$$

where  $\boldsymbol{\theta}_{Nx1}$  is a vector representing the target flip angle at each voxel,  $\mathbf{A}_{LCLTA}$  is the  $N \times M$  system matrix representing the conjugate of the transmit field sensitivities and the Fourier kernel  $e^{-ir \cdot \mathbf{k}(t)}$  and  $\mathbf{x}_{M \times 1}^*$  is the conjugate of the RF pulse.

The LCLTA algorithm is very similar to the STA algorithm except the requirement that the pulse should be composable of a sequence of inherently refocused small excitation pulses. This requirement is not very strict in the sense that even if the sub-pulses are approximately inherently refocused the algorithm can still work.

Despite the simplicity of the LCLTA method, its bad performance at larger tip angles, e.g. 180°, required the development of more accurate and possibly nonlinear design methods for large tip angle pulses. As mentioned earlier, there have been several successful approaches to large tip angle pulse design and among these to our best knowledge none of them explicitly incorporates the SAR constraints into their designs. Instead, they indirectly control SAR through peak RF voltage to satisfy the safety limits. In this section we will explain the development of a SAR constrained large tip angle pulse design method which we will refer to as the full Bloch simulation method, based on a modification of the nonlinear composite pulses approach developed by Gumbrecht (24).

## 3.2 Full Bloch Simulation Method

The full Bloch simulation method is developed in the spinor domain. As mentioned earlier, the Bloch equation in the rotating frame neglecting the relaxations is

$$\begin{pmatrix} \dot{M}_x \\ \dot{M}_y \\ \dot{M}_z \end{pmatrix} = \gamma \begin{pmatrix} 0 & \mathbf{G} \cdot \mathbf{r} & -B_{1,y} \\ -\mathbf{G} \cdot \mathbf{r} & 0 & B_{1,x} \\ B_{1,y} & -B_{1,x} & 0 \end{pmatrix} \begin{pmatrix} M_x \\ M_y \\ M_z \end{pmatrix} \quad (3.8)$$

The solution to this equation is a rotation

$$\mathbf{M}(T) = \mathbf{R}\mathbf{M}(0) \quad (3.9)$$

where R is a 3x3 orthonormal matrix. This rotation can also be represented by a 2x2 unitary matrix

$$\mathbf{Q} = \begin{pmatrix} \alpha & -\beta^* \\ \beta & \alpha^* \end{pmatrix} \quad (3.10)$$

where  $\alpha$  and  $\beta$  are the Cayley Klein parameters

$$\alpha = \cos\left(\frac{\theta}{2}\right) - in_z \sin\left(\frac{\theta}{2}\right) \quad (3.11)$$

$$\beta = -i(n_x + in_y) \sin\left(\frac{\theta}{2}\right) \quad (3.12)$$

$\theta$  is the tip angle whereas the  $\mathbf{n}$  vector is the axis of rotation. The spin domain matrices can be used to find the effect of RF in the presence of a constant gradient field. Hence, the pulse is sampled and the total effect of the pulse is the multiplication of the rotation matrices due to each sample in order.

$$\mathbf{Q} = \mathbf{q}_n \mathbf{q}_{n-1} \cdots \mathbf{q}_1 \quad (3.13)$$

With the spin domain representation of the rotation in hand, it is easy to invert back to the 3x3 rotation matrix to find the magnetization

$$\begin{pmatrix} M_{xy}^+ \\ M_{xy}^{+*} \\ M_z^+ \end{pmatrix} = \begin{pmatrix} (\alpha^*)^2 & -\beta^2 & 2\alpha^*\beta \\ -(\beta^*)^2 & \alpha^* & 2\alpha\beta^* \\ -\alpha^*\beta^* & -\alpha\beta & \alpha\alpha^* - \beta\beta^* \end{pmatrix} \begin{pmatrix} M_{xy}^- \\ M_{xy}^{-*} \\ M_z^- \end{pmatrix} \quad (3.14)$$

where  $M_{xy} = M_x + iM_y$ .

The target function of the optimization algorithm can be determined from Equation (3.14) depending on the application. There are three major large tip angle applications: excitation, inversion and spin echo.

*Excitation:* In case of excitation, initial magnetization is  $M^- = (0 \ 0 \ M_0)$  and the magnetization of interest is the transverse magnetization. Hence the target function is

$$M_{xy}^+ = 2\alpha^*\beta M_0 \quad (3.15)$$

Sometimes the phase of the magnetization matters while in most cases only the magnitude is important provided that the phase varies slowly enough not to cancel out or distort the MRI signal inside one voxel. In such cases the target function becomes  $|M_{xy}^+| = |2\alpha^* \beta M_0|$ .

*Inversion:* The initial magnetization is the same as in the excitation case while the magnetization of interest is not the transverse magnetization but the longitudinal one since the objective in inversion is to invert the magnetization along +z into -z. Hence the target function is

$$M_z^+ = (\alpha\alpha^* - \beta\beta^*)M_0 \quad (3.16)$$

*Refocusing:* The goal in a refocusing pulse is to rotate all spins around a rotation axis on the transverse plane by  $180^\circ$ . Hence the initial magnetization is an arbitrary magnetization on the transverse plane  $M^- = (M_x^- \ M_y^- \ 0)$ . Practically, a refocusing pulse is usually surrounded by crusher gradients to eliminate the effects of parasitic signals. Crusher gradients are correction gradients that preserve only the desired signals by manipulating the phase of the signals. One crusher gradient lobe causes a rotation by

$$\varphi(r) = r \left( 2\pi\gamma \int G(t) dt \right) \quad (3.17)$$

This rotation can be represented by the following rotation matrix

$$R_c = \begin{pmatrix} e^{-i\varphi(r)/2} & 0 \\ 0 & e^{i\varphi(r)/2} \end{pmatrix} \quad (3.18)$$

Combining the rotation matrices of the left crusher gradient lobe, the RF waveform and the right crusher gradient lobe, the total rotation matrix is

$$R_{total} = R_c R_{RF} R_c \quad (3.19)$$

$$= \begin{pmatrix} \alpha e^{-i\varphi(r)} & -\beta^* \\ \beta & \alpha^* e^{i\varphi(r)} \end{pmatrix} \quad (3.20)$$

Hence the transverse magnetization after the application of the RF pulse is

$$M_{xy}^+ = (\alpha^*)^2 e^{i2\varphi(r)} M_{xy}^- - \beta^2 M_{xy}^{-*} + 2\alpha^* e^{i\varphi(r)} \beta M_z^- \quad (3.21)$$

If the crusher gradients' area is large enough so that  $\varphi(r)$  varies by at least  $4\pi$  across one voxel then the first and the last terms in Equation (3.21) cancel out due to the integration and we are left with

$$M_{xy}^+ = -\beta^2 M_{xy}^{-*} \quad (3.22)$$

See (25) for a more complete discussion on refocusing pulses. Assume the initial magnetization makes an angle of  $\varphi_0$  with the x axis while the rotation axis for the spins makes an angle of  $\varphi_r$ .

$$M_{xy}^- = M e^{i\varphi_0} \quad (3.23)$$

$$M_{xy}^+ = M e^{i(2\varphi_r - \varphi_0)} \quad (3.24)$$

$$= M_{xy}^{-*} e^{i2\varphi_r} \quad (3.25)$$

Combining equation (3.22) with equation (3.25) we obtain the objective function (left) and target value (right) of a refocusing pulse

$$\beta^2 = -e^{i2\varphi_r} \quad (3.26)$$

Having determined the target function for the three major cases, we can now describe the full Bloch simulation method in steps:

*Step 1:* The basis of the algorithm is the following minimization

$$\min_x y = \sum_{i=1}^N |T_i(x) - T_i^{target}|^2 \quad (3.27)$$

where  $x$  is the RF,  $N$  is the number of voxels,  $T_i$  is the objective function at voxel  $i$  and  $T_i^{target}$  is the target value at voxel  $i$ . The target function and values for the three cases discussed above are:

- For the excitation case,  $T(x) = M_{xy}^+ = 2\alpha^*\beta M_0$  and  $T^{target} = \sin(\theta)$  where  $\theta$  is the target flip angle
- For the inversion case,  $T(x) = M_z^+ = \alpha\alpha^* - \beta\beta^*$  and  $T^{target} = -1$
- For the refocusing case,  $T(x) = \beta^2$  and  $T^{target} = -e^{i2\varphi_r}$

*Step 2:* Next, we need the derivative of  $y$  with respect to the real and imaginary parts of RF at each individual transmit channel.

$$\frac{\partial y}{\partial x_{c,t,r}} = \sum_{i=1}^N \left[ \frac{\partial T_i(x)}{\partial x_{c,t,r}} (T_i(x) - T_i^{target}(x))^* + \frac{\partial T_i(x)^*}{\partial x_{c,t,r}} (T_i(x) - T_i^{target}(x)) \right] \quad (3.28)$$

where  $x_{c,t,r}$  is the real part of the RF waveform at channel  $c$  at time  $t$  ( $x_{c,t,i}$  for the imaginary part).  $T_i(x) - T_i^{target}(x)$  can be found by finding the Cayley-Klein parameters  $\alpha$  and  $\beta$  after running a full Bloch simulation.  $\frac{\partial T_i(x)}{\partial x_{c,t,r}}$  is different for the three cases we discussed above:

- For excitation:

$$\frac{\partial T_i(x)}{\partial x_{c,t,r}} = 2M_0 \left[ \frac{\partial \alpha_i^*(x)}{\partial x_{c,t,r}} \beta_i(x) + \alpha_i^*(x) \frac{\partial \beta_i(x)}{\partial x_{c,t,r}} \right] \quad (3.29)$$

- For inversion:

$$\frac{\partial T_i(x)}{\partial x_{c,t,r}} = M_0 \left[ \frac{\partial \alpha_i^*(x)}{\partial x_{c,t,r}} \alpha_i(x) + \alpha_i^*(x) \frac{\partial \alpha_i(x)}{\partial x_{c,t,r}} - \frac{\partial \beta_i^*(x)}{\partial x_{c,t,r}} \beta_i(x) - \beta_i^*(x) \frac{\partial \beta_i(x)}{\partial x_{c,t,r}} \right] \quad (3.30)$$

- For refocusing:



$$\frac{\partial T_i(x)}{\partial x_{c,t,r}} = 2\beta_i(x) \frac{\partial \beta_i(x)}{\partial x_{c,t,r}} \quad (3.31)$$

Since  $\alpha_i(x)$  and  $\beta_i(x)$  are already found during the Bloch simulation, only their derivatives are to be calculated. The total spin matrix for one voxel is defined as

$$\mathbf{Q}_i(x) = \begin{pmatrix} \alpha_i(x) & -\beta_i^*(x) \\ \beta_i(x) & \alpha_i^*(x) \end{pmatrix} = \mathbf{q}_{i,T} \mathbf{q}_{i,T-1} \cdots \mathbf{q}_{i,2} \mathbf{q}_{i,1} \quad (3.32)$$

Then only one of the spin matrices will depend on  $x_{c,t,r}$ , that is  $\mathbf{q}_{i,t}$ . Therefore

$$\frac{\partial \mathbf{Q}_i(x)}{\partial x_{c,t,r}} = \begin{pmatrix} \frac{\partial \alpha_i(x)}{\partial x_{c,t,r}} & -\frac{\partial \beta_i^*(x)}{\partial x_{c,t,r}} \\ \frac{\partial \beta_i(x)}{\partial x_{c,t,r}} & \frac{\partial \alpha_i^*(x)}{\partial x_{c,t,r}} \end{pmatrix} = \mathbf{q}_{i,T} \mathbf{q}_{i,T-1} \cdots \mathbf{q}_{i,t+1} \frac{\partial \mathbf{q}_{i,t}}{\partial x_{c,t,r}} \mathbf{q}_{i,t-1} \cdots \mathbf{q}_{i,2} \mathbf{q}_{i,1} \quad (3.33)$$

$$\frac{\partial \mathbf{q}_{i,t}}{\partial x_{c,t,r}} = \begin{pmatrix} \frac{\partial a_{i,t}}{\partial x_{c,t,r}} & -\frac{\partial b_{i,t}^*}{\partial x_{c,t,r}} \\ \frac{\partial b_{i,t}}{\partial x_{c,t,r}} & \frac{\partial a_{i,t}^*}{\partial x_{c,t,r}} \end{pmatrix} \quad (3.34)$$

Using the definition of the Cayley-Klein parameters

$$a_{i,t} = \cos(\varphi_{i,t}/2) - in_{z,i,t} \sin(\varphi_{i,t}/2) \quad (3.35)$$

$$b_{i,t} = -i(n_{x,i,t} + in_{y,i,t}) \sin(\varphi_{i,t}/2) \quad (3.36)$$

their derivatives can be calculated as the following

$$\frac{\partial a_{i,t}}{\partial x_{c,t,r}} = -0.5 \sin(\varphi_{i,t}/2) \frac{\partial \varphi_{i,t}}{\partial x_{c,t,r}} - 0.5 in_{z,i,t} \cos(\varphi_{i,t}/2) \frac{\partial \varphi_{i,t}}{\partial x_{c,t,r}} - i \frac{\partial n_{z,i,t}}{\partial x_{c,t,r}} \sin(\varphi_{i,t}/2) \quad (3.37)$$

$$\frac{\partial b_{i,t}}{\partial x_{c,t,r}} = -0.5i(n_{x,i,t} + in_{y,i,t}) \cos(\varphi_{i,t}/2) \frac{\partial \varphi_{i,t}}{\partial x_{c,t,r}} - i \left( \frac{\partial n_{x,i,t}}{\partial x_{c,t,r}} + i \frac{\partial n_{y,i,t}}{\partial x_{c,t,r}} \right) \sin(\varphi_{i,t}/2) \quad (3.38)$$

The rotation angle and the rotation axis can be found using the RF and gradient fields:

$$\varphi_{i,t} = -2\pi\gamma\Delta t \sqrt{|B_{1,i,t}|^2 + (G \cdot r_i)^2} \quad (3.39)$$

$$n_{i,t} = \frac{(B_{1,x,i,t}, B_{1,y,i,t}, G \cdot r_i)}{\sqrt{|B_{1,i,t}|^2 + (G \cdot r_i)^2}} \quad (3.40)$$

Since  $G \cdot r_i = 0$  during the RF sub-pulses, their derivatives can be calculated as

$$\frac{\partial \varphi_{i,t}}{\partial x_{c,t,r}} = -2\pi\gamma\Delta t \frac{1}{|B_{1,i,t}|} \left[ B_{1,x,i,t} \frac{\partial B_{1,x,i,t}}{\partial x_{c,t,r}} + B_{1,y,i,t} \frac{\partial B_{1,y,i,t}}{\partial x_{c,t,r}} \right] \quad (3.41)$$

$$\frac{\partial n_{x,i,t}}{\partial x_{c,t,r}} = \frac{\frac{\partial B_{1,x,i,t}}{\partial x_{c,t,r}} |B_{1,i,t}|^2 - B_{1,x,i,t} \left[ B_{1,x,i,t} \frac{\partial B_{1,x,i,t}}{\partial x_{c,t,r}} + B_{1,y,i,t} \frac{\partial B_{1,y,i,t}}{\partial x_{c,t,r}} \right]}{|B_{1,i,t}|^3} \quad (3.42)$$

$$\frac{\partial n_{y,i,t}}{\partial x_{c,t,r}} = \frac{\frac{\partial B_{1,y,i,t}}{\partial x_{c,t,r}} |B_{1,i,t}|^2 - B_{1,y,i,t} (B_{1,x,i,t} \frac{\partial B_{1,x,i,t}}{\partial x_{c,t,r}} + B_{1,y,i,t} \frac{\partial B_{1,y,i,t}}{\partial x_{c,t,r}})}{|B_{1,i,t}|^3} \quad (3.43)$$

$$\frac{\partial n_{z,i,t}}{\partial x_{c,t,r}} = 0 \quad (3.44)$$

since  $G \cdot r_i = 0$  during the RF subpulses. Using the definition of the x and y components of the transmit fields in a parallel transmission system

$$B_{1,x,i,t} = \text{Re} \left\{ \sum_{c=1}^C B_{1,i,c} x_{c,t} \right\} \quad (3.45)$$

$$B_{1,y,i,t} = \text{Im} \left\{ \sum_{c=1}^C B_{1,i,c} x_{c,t} \right\} \quad (3.46)$$

Their derivatives can be determined by using the transmit field maps directly as follows

$$\frac{\partial B_{1,x,i,t}}{\partial x_{c,t,r}} = \text{Re}\{B_{1,i,c}\} \quad (3.47)$$

$$\frac{\partial B_{1,y,i,t}}{\partial x_{c,t,r}} = \text{Im}\{B_{1,i,c}\} \quad (3.48)$$

$$\frac{\partial B_{1,x,i,t}}{\partial x_{c,t,i}} = -\text{Im}\{B_{1,i,c}\} \quad (3.49)$$

$$\frac{\partial B_{1,y,i,t}}{\partial x_{c,t,i}} = \text{Re}\{B_{1,i,c}\} \quad (3.50)$$

Having defined the derivative of the objective function, the SAR and RF power constraints can be added to the optimization in order to complete the algorithm;

$$\min_x \sum_{i=1}^N |T_i(x) - T_i^{target}|^2 \quad (3.51)$$

$$\text{s.t.} \quad |x_c(t)| < x_{\max} \quad \forall c, t \quad (3.52)$$

$$\text{SAR}(\vec{r}) \approx \frac{\sigma(\vec{r})}{2\rho(\vec{r})} \left\{ \frac{T_{RFsub}}{T_{RF}} \sum_{k=1}^K \mathbf{x}^H \mathbf{Q}(\vec{r}) \mathbf{x} \right\} < \text{SAR}_{\max} \quad \forall \vec{r} \quad (3.53)$$

If one wants to optimize only the magnitude profile then Equation (3.51) needs to be modified in the following way:

$$\min_x \sum_{i=1}^N (|T_i(x)| - |T_i^{target}|)^2 \quad (3.54)$$

The structure of the optimization algorithm for the large tip angle full Bloch simulation method is very similar to both STA and LCLTA methods. The incorporation of the SAR and RF power constraints is the same whereas the objective function changes. Since the problem is no longer convex, the outcome of this optimization will be a local minimum. This means the starting point of the algorithm plays a crucial role in reaching a fairly good final point. In this work, a two-step pulse design process is adopted. In the first step, an LCLTA algorithm is used to design an RF pulse with a relatively close magnetization profile to that of the target. In the second step, this RF pulse is used as the initial point to the full Bloch simulation method. Obviously, the results presented in the next section depend not only on the capabilities and the performance of the full Bloch simulation but also on how good of an initial point is fed into it, and therefore the performance of the LCLTA algorithm.

### 3.3 Simulation Data

The full Bloch simulation method was tested using electromagnetic simulations of a 7 T, 8-channel transmit array loaded with a 33 tissue types body model (26). The axial, sagittal and coronal visualization of the simulated data set can be seen in Figure 8. The transmit field sensitivities ( $B_1^+$  maps) of the individual channels inside a slice right above the sinus cavity are plotted in Figure 9.

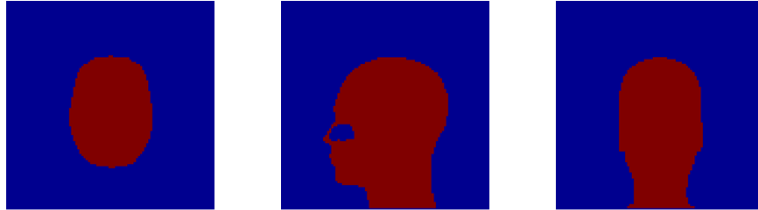


Figure 8: The axial, sagittal and coronal (from left to right) visualization of the simulation data set

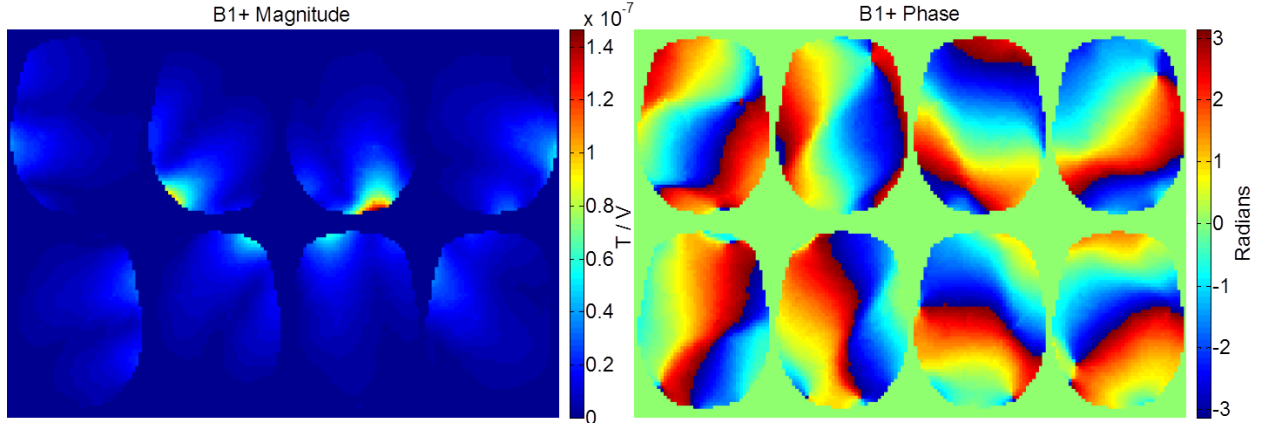


Figure 9: The magnitude and phase profiles of the individual channels through a slice right above the sinus cavity

### 3.4 Error Metrics

Throughout the next section, multiple error metrics will be used to assess and compare the performances of several RF pulses. These error metrics are defined here.

RMMSE (%) is the main error metric used to refer to the root magnitude mean square error in percentage of the mean of the target magnetization. This error metric is used to quantify the magnitude profile error. It implicitly indicates both how close the magnitude mean of the simulated magnetization is to the target mean and how much variation there is across the volume of interest. It is defined as:

$$RMMSE (\%) = \frac{\sqrt{\sum_{i=1}^N (|m_i^{sim}| - |m_i^{target}|)^2}}{\sum_{i=1}^N |m_i^{target}|} * 100 \quad (3.55)$$

where  $m_i^{sim}$  refers to the simulated magnetization at voxel  $i$ ,  $m_i^{target}$  refers to the target magnetization at voxel  $i$  and  $N$  is the number of voxels in the volume of interest.

RMSE (%) is the metric used to refer to the root mean square error in percentage of the mean of the target magnetization. It quantifies both the magnitude and the phase profile errors unlike the RMMSE which only quantifies the magnitude profile error. As previously mentioned, for most cases only the magnitude profile matters but in the case of inversion pulses, the error has to be expressed in terms of RMSE rather than RMMSE. This is because an inversion pulse targets to tip the spins by  $180^\circ$  from magnetization state  $(0,0,1)$  to  $(0,0,-1)$ , referring to magnetization components on  $x$ ,  $y$  and  $z$  axes. If only the magnitude profile is checked for an inversion pulse, there would be no difference between a correctly tipped spin and an untouched spin. RMSE (%) is defined as:

$$RMSE (\%) = \frac{\sqrt{\sum_{i=1}^N (|m_i^{sim} - m_i^{target}|)^2}}{\sum_{i=1}^N |m_i^{target}|} * 100 \quad (3.56)$$

Mag mean is the mean of the resulting magnetization magnitude profile. It has no units and is defined as:

$$Mag\ mean = \frac{\sum_{i=1}^N |m_i^{sim}|}{N} \quad (3.57)$$

Phase mean (°) is the mean of the resulting magnetization phase profile. It is in units of degrees and is defined as:

$$Phase\ mean\ (^{\circ}) = \frac{\sum_{i=1}^N \angle m_i^{sim}}{N} \quad (3.58)$$

Norm Mag Std (%) is the normalized standard deviation of the simulated magnitude profile in percentage of the mean of the target magnitude profile. It is defined as:

$$Norm\ Mag\ Std(\%) = \frac{\sqrt{\sum_{i=1}^N (|m_i^{sim}| - |m_i^{target}|)^2}}{N} * 100 \quad (3.59)$$

Phase Std (°) is the standard deviation of the phase profile. It is in units of degrees.

Dev 10% (%) is the percentage of the voxels whose magnetization magnitude is in the 10% range of the target magnetization magnitude.

Dev 20% (%) is the percentage of the voxels whose magnetization magnitude is in the 20% range of the target magnetization magnitude.

Mag mean and phase mean indicate how close the overall resulting magnetization is to the target while the Norm Mag Std and Phase Std indicate how homogeneous the resulting magnetization is. RMMSE (or RMSE) % is an indicator of errors in both the magnitude (or magnitude and phase) mean and homogeneity of the resulting magnetization. Dev 10% and Dev 20% are just other forms of error quantification that can be used to further evaluate the performance of the RF pulse. These error criteria are not completely independent of each other but yet are simultaneously used to better assess the performance of an RF pulse and more thoroughly compare different RF pulses in the next section. In the cases where only one criterion needs to be chosen, RMMSE % (RMSE % for inversion pulses) is used since it is the most comprehensive error quantifier among others described above.

## 4 Results

In this section, the performance of the full Bloch simulation pulse design algorithm will be demonstrated for several cases. First of all, some of the widely accepted claims that were mentioned in the previous sections about pulse design (such as the need for pulse design at high field systems, the need for a large tip angle pulse design algorithm, etc.) will be showcased in order to provide a more complete understanding of the algorithm and construct its reliability. Then, the conventional least squares algorithm will be compared with the magnitude least squares algorithm. Finally, the results of the constrained pulse design using the full Bloch simulation method at large tip angle will be presented and the algorithm will be analyzed by varying several parameters. Throughout this section, the results of small tip angle regime will be compared with the ones of large tip angle regime for a more thorough understanding whenever necessary.

### 4.1 Pulse Design

As explained earlier, the central brightening effect distorts the homogeneity of the RF transmit field at higher field MRI systems requiring users to design RF pulses that can mitigate the inhomogeneities. In this section several stages of pulse design are compared for both small tip angle and large tip angle cases. In addition, the performances of the STA algorithm, the LCLTA algorithm and the full Bloch algorithm are evaluated at large target tip angles.

#### 4.1.1 Pulse Design at Small Tip Angle

In a single channel system all the channels in the coil play the same waveform with a predetermined phase shift between them. The only parameters the RF designer can control about the waveform are the amplitude and the duration of the waveform. With this configuration, the central brightening effect occurs as seen in Figure 10 (leftmost). This mode which we call as the BC mode refers to the circularly polarized birdcage mode of a pTx coil where the conventional birdcage coil is imitated. The waveforms are chosen to be rectangular. The second level in pulse design with  $k_T$ -points trajectory is the RF shimming case where we have only 1  $k_T$ -point at the origin of the excitation  $k$ -space and the RF waveforms of all channels are rectangular with varying amplitude and phases. With more degrees of freedom in hand, a more homogeneous excitation profile is expected for RF shimming than BC mode and a slight improvement can be observed in the magnitude profile (RMMSE of 37% for RF Shimming vs 40% for BC mode). The mean of the resulting phase is also much closer to the target phase when

compared to the BC mode phase. When more  $k_T$ -points are added the shapes of the waveforms played through different channels become different, giving us even more degrees of freedom. It can be seen Figure 10 that moving from 1  $k_T$ -point to 2  $k_T$ -points, there is a drastic improvement in the phase profile as well as the magnitude profile and the excitation fidelity gets better as the number of  $k_T$ -points increase. Since the duration of RF energy emission at one  $k_T$ -point is kept constant (constant RF sub-pulse duration), the whole RF pulse duration increases as the number of  $k_T$ -points increase. Hence there is a tradeoff between the excitation fidelity and the pulse duration.

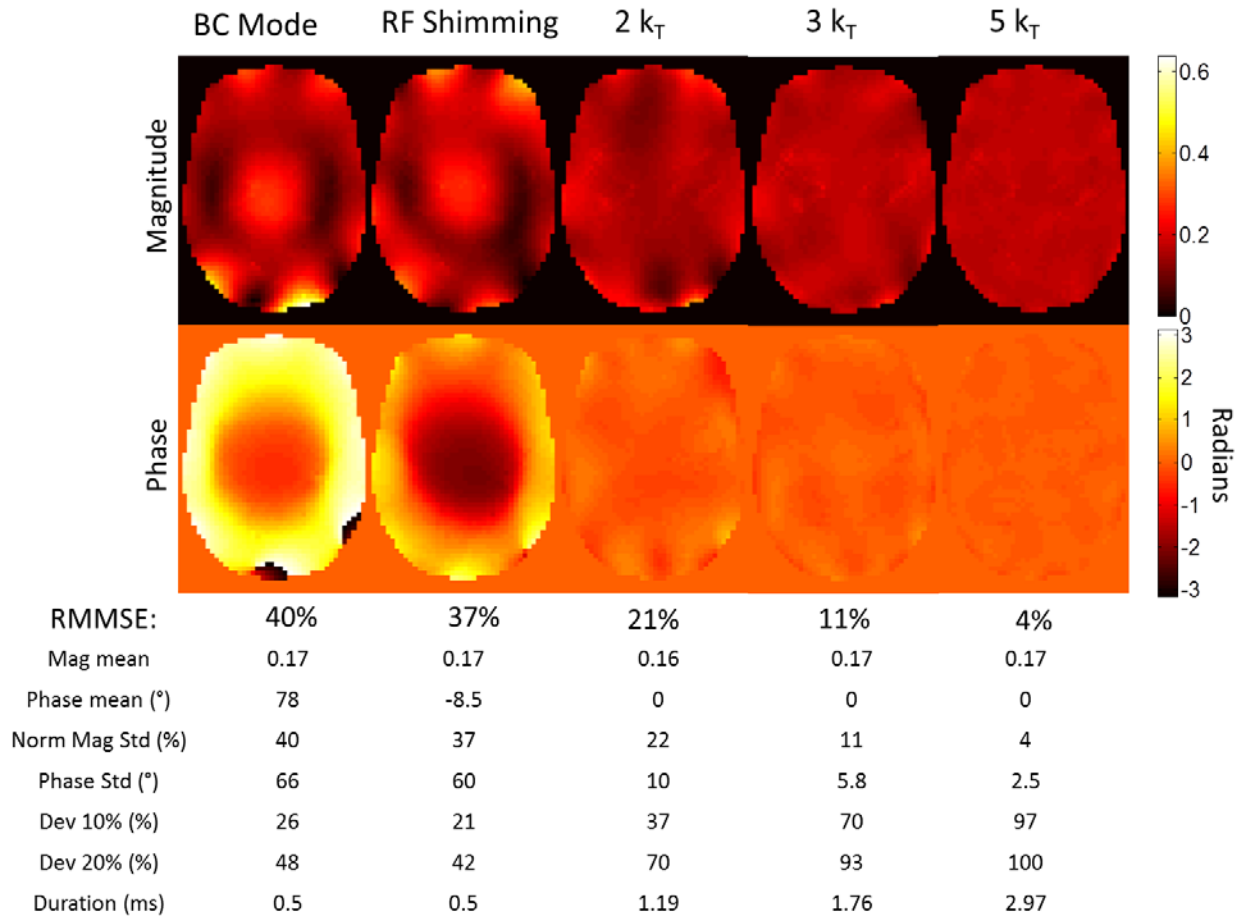


Figure 10: The comparison between circularly polarized birdcage mode, RF shimming (1  $k_T$ -point), 2  $k_T$ -points, 3  $k_T$ -points and 5  $k_T$ -points cases at small tip angle using the small tip angle approximation method introduced in the Background section with a least squares algorithm. Target tip angle:  $10^\circ$  (target magnetization: 0.17), target phase: flat  $0^\circ$ .

Table 1: The peak RF voltage, peak 10g local SAR and global SAR values of the pulses in Figure 10. A duty cycle of 10% was assumed.

	BC Mode	RF Shimming	2 kt	3 kt	5kt
Peak RF (V)	35	66	57	61	78
Peak 10g LSAR (W/kg)	0.38	0.67	0.28	0.18	0.21
GSAR (W/kg)	0.07	0.09	0.03	0.03	0.06

#### 4.1.2 Small Tip Angle Pulse Design vs Large Tip Angle Pulse Design

As mentioned in the Background section, the small tip angle approximation assumes that the tip angle is small such that the longitudinal component of the magnetization can be approximated as constant over time. As the tip angle increases, this assumption no longer holds and the pulses designed with the STA approximation method no longer work as expected. To illustrate this phenomenon, idealistic  $B_1^+$  maps which are perfectly homogeneous are constructed and RF pulses with a flat target excitation profile are designed using the STA approximation method with a least squares algorithm for target tip angles between  $10^\circ$  and  $90^\circ$ . The target magnetization as well as the mean and the standard deviation of the STA approximation model and the Bloch simulation results for all target tip angles can be found in Figure 11. The STA approximation model here refers to Equation (2.15) and is the prediction of the STA approximation method. However, the actual effect of the RF is given by the Bloch simulation and as Figure 11 shows, the Bloch simulation results do not agree with the STA approximation model prediction. This, as expected, means the STA approximation does not hold at larger tip angles (after around  $30^\circ$ ) and some other algorithm is needed to design pulses at these tip angles. Note that zero standard deviations for all designs implies that the difference between the mean of the Bloch simulation and the mean of the STA approximation model is not due to the imperfection of the optimizing algorithm but the inaccuracy of the STA approximation model.



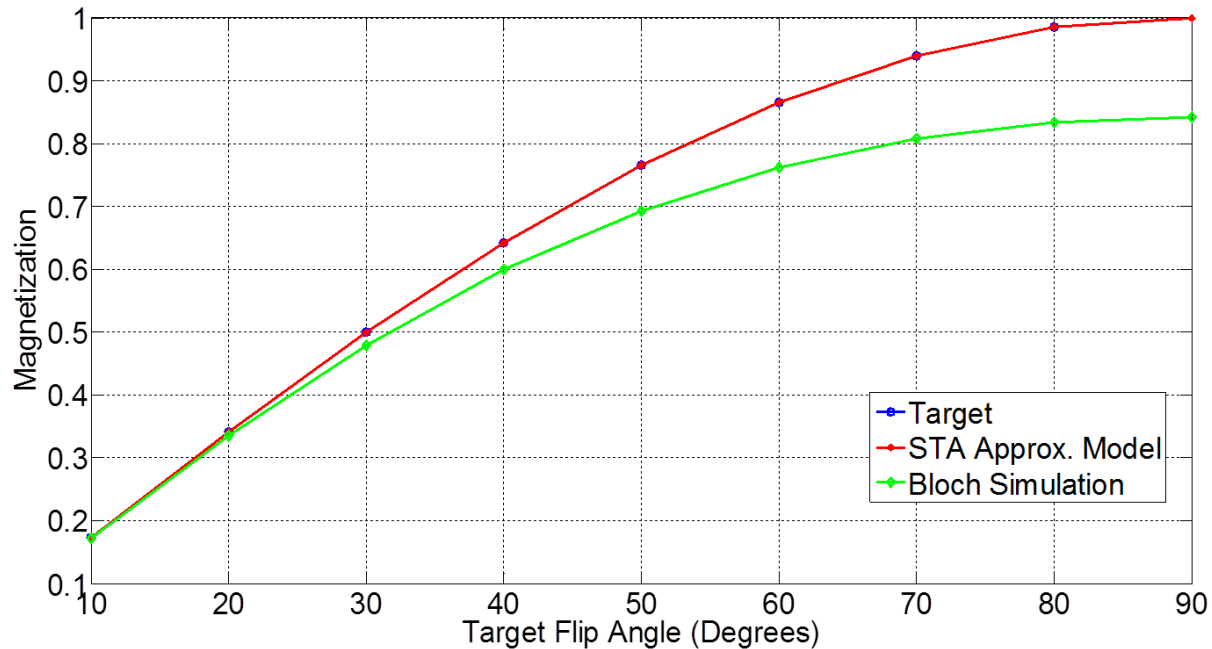


Figure 11: The mean and the standard deviations of the magnetizations of the target, STA approximation model ( $A \cdot b$  in Equation (2.15)) and the Bloch simulation for tip angles between  $10^\circ$  and  $90^\circ$ . A least squares algorithm was used with 1  $k_T$ -point. Target phase: flat  $0^\circ$ , volume of interest: a slice of thickness 4 mm, RF pulse duration: 0.5 ms. Perfectly homogenous  $B_1^+$  maps were used.

Linear class of large tip angle (LCLTA) pulses have been previously suggested for large tip angle pulse design. LCLTA method is a generalization of the STA method which works well at large tip angles unlike the STA method but has some assumptions about the RF pulse and the k-space trajectory accompanying it. To assess the performance of the LCLTA method at large tip angles, again imaginary  $B_1^+$  maps that are perfectly homogeneous are constructed and RF pulses with a flat target excitation profile are designed using the LCLTA method for target tip angles varying between  $10^\circ$  and  $180^\circ$ . The mean and the standard deviation of the magnetization for both the target and the Bloch simulation results can be seen in Figure 12. With perfect transmit field maps the LCLTA method results in perfect excitation fidelity achieving the target mean with zero standard deviations for all target tip angles.

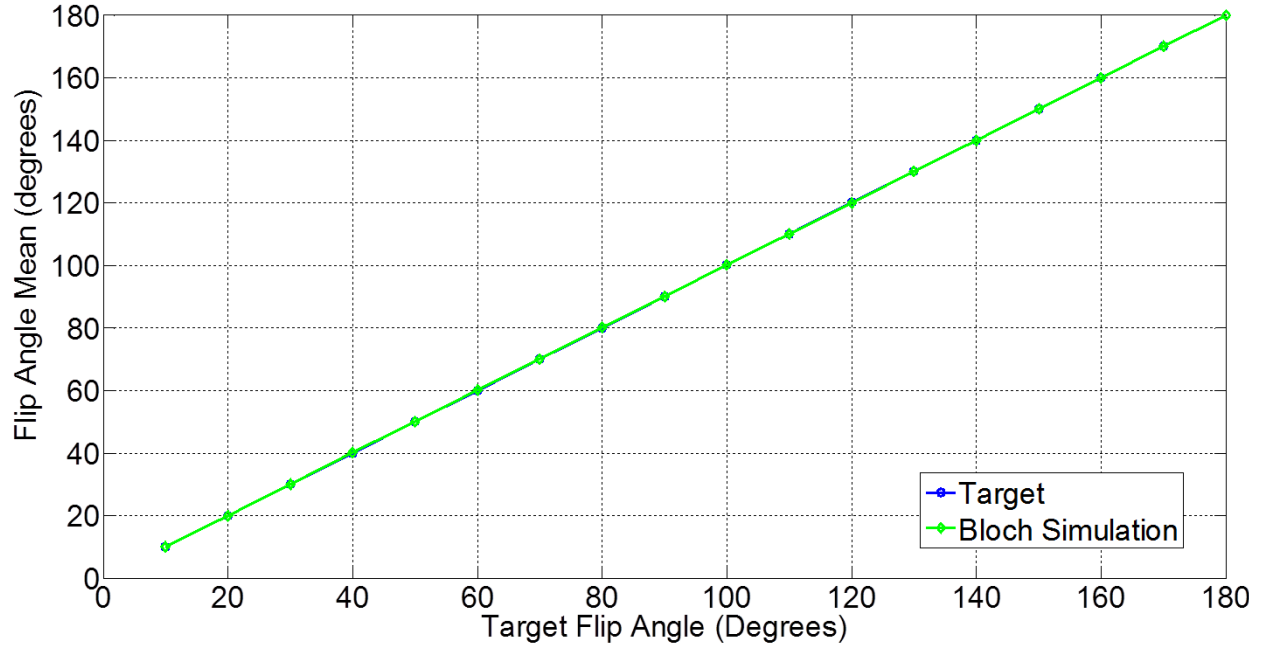


Figure 12: The mean and the standard deviations of the magnetizations of the target and the Bloch simulation for the LCLTA design for target tip angles between  $10^\circ$  and  $180^\circ$ . A least squares algorithm was used with 1  $k_T$ -point. The target phase: flat  $0^\circ$ , volume of interest: a slice of thickness 4 mm, RF pulse duration: 0.5 ms. Perfectly homogenous  $B_1^+$  maps were used.

The next step is to test the LCLTA method with the realistic  $B_1^+$  maps and the results of the same configuration as in Figure 12 except that the realistic  $B_1^+$  maps were used can be seen in Figure 13. Obviously, LCLTA method performs poorly for the case of  $k_T$ -points with realistic  $B_1^+$  maps. It is important to note that this poor performance is not only caused by the incompatibility of the LCLTA method with  $k_T$ -point pulses (the fact that the  $k_T$ -points trajectory does not satisfy all the assumptions of the LCLTA pulses) but also the performance of the least squares algorithm used, the number of  $k_T$ -points and other parameters in the design procedure. One of the most important assumptions of LCLTA pulses is the small excitation assumption which requires the effect of the RF to be small. This assumption may not be thoroughly satisfied in case of  $k_T$ -points since the RF waveform and the gradient waveforms are non-overlapping and when the RF waveform is played there is no gradient in effect. As a result, the performance of the LCLTA algorithm for  $k_T$ -points trajectory in Figure 13 is much worse than the demonstrated performance of the algorithm in (19) for spokes trajectory. Nevertheless, it is only fair to claim that the LCLTA method requires the pulses to be of a specific type and therefore is a fairly limited pulse design method. Furthermore, it is unable to achieve acceptable excitation profiles especially for target tip angles around  $180^\circ$ .

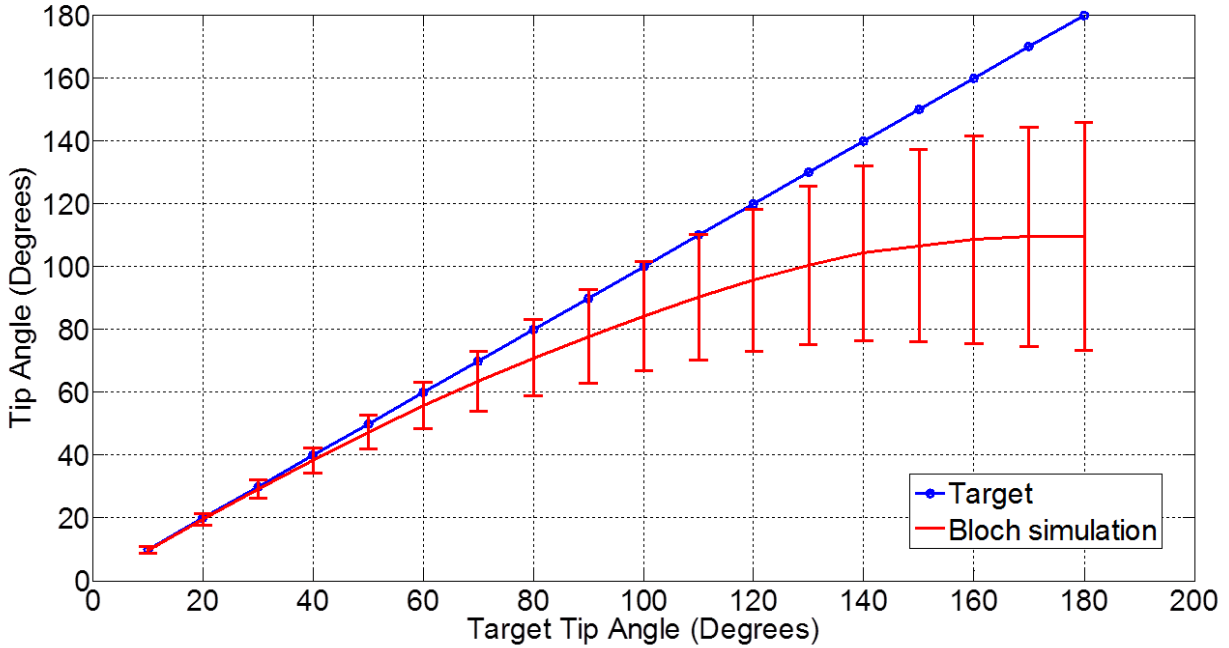


Figure 13: The mean and the standard deviations of the magnetizations of the target and the Bloch simulation of the LCLTA design for target tip angles between  $10^\circ$  and  $180^\circ$ . A least squares algorithm was used with 9  $k_T$ -points. The target phase: flat  $0^\circ$ , volume of interest: a slice of thickness 4 mm, RF pulse duration 5.29 ms. Realistic  $B_1^+$  maps were used.

The full Bloch simulation method developed in the Methods section has no assumptions on the k-space trajectory or the RF pulse hence it is a more general large tip angle pulse design method. Unlike the STA approximation or the LCLTA methods, the full Bloch simulation is a non-convex method. Thus the initial point fed into the algorithm is crucial in reaching a good final point due to the fact that the final point will be a local optimal point that is in the neighborhood of the initial point. Using the output of the LCLTA method as the initial point of the full Bloch simulation method was suggested in the Methods section. Testing the performance of this two-step pulse design algorithm with realistic  $B_1^+$  maps, the results shown in Figure 14 are obtained. The instant drop in the mean of the simulated magnetization near  $180^\circ$  is most probably due to a poor initial point and further emphasizes the significance of a good starting point for the full Bloch simulation method.

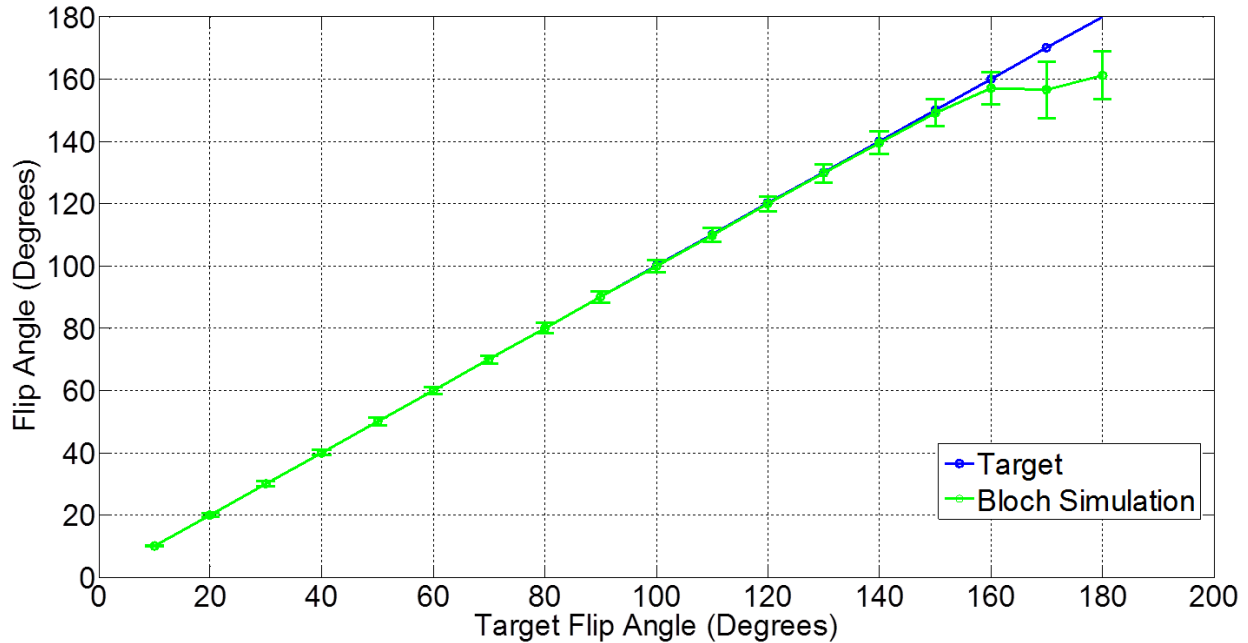


Figure 14: The mean and the standard deviations of the magnetizations of the target and the Bloch simulation for the full Bloch simulation design for target tip angles between  $10^\circ$  and  $180^\circ$ . A least squares algorithm was used with 9  $k_T$ -points. The target phase:  $0^\circ$ , volume of interest: a slice of thickness 4 mm, RF pulse duration 5.29 ms. Realistic  $B_1^+$  maps were used.

### 4.1.3 Pulse Design at Large Tip Angle

In this section the results in section “Pulse Design at Small Tip Angle” are reproduced for target flip angles of  $90^\circ$  and  $180^\circ$  to observe the performance of the full Bloch simulation method visually and to prove that SAR constrained pulse design becomes more and more critical as the tip angle increases.

A similar pattern to the excitation profiles for the small tip angle case (Figure 10) can be observed for  $90^\circ$  excitation and  $180^\circ$  inversion pulses. (Figure 15, Figure 16). On the other hand, if Table 1, Table 2 and Table 3 are compared, it is prominent that as the target tip angle gets larger the required RF voltage value as well as the local SAR and global SAR values increase. In fact, these values are higher than the hardware and the safety limits for most of the cases of unconstrained  $90^\circ$  excitation and  $180^\circ$  inversion pulses. As a result, the ability to mitigate the  $B_1^+$  inhomogeneity when subject to peak RF voltage and SAR limitations at large tip angle regime is much more crucial than it is at small tip angle regime.

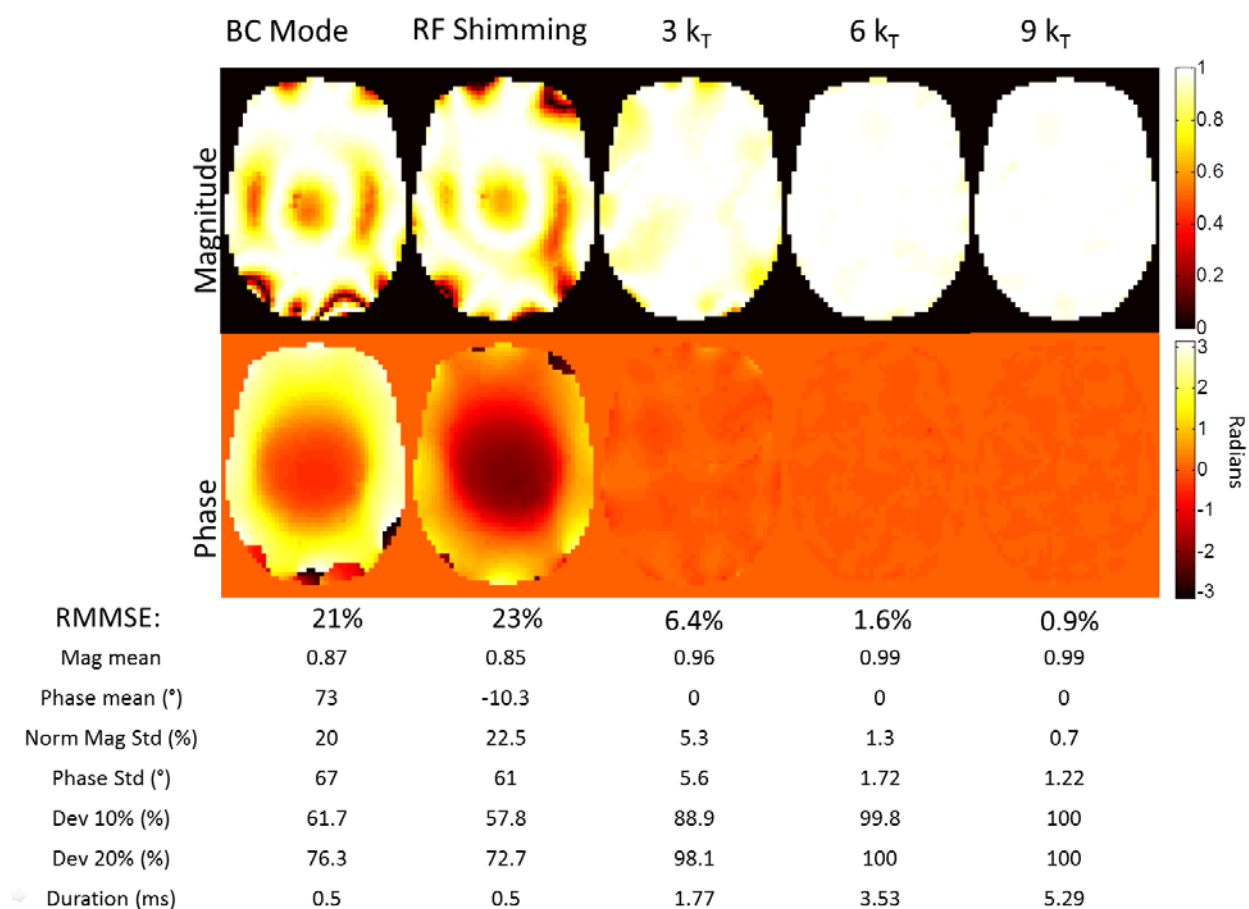
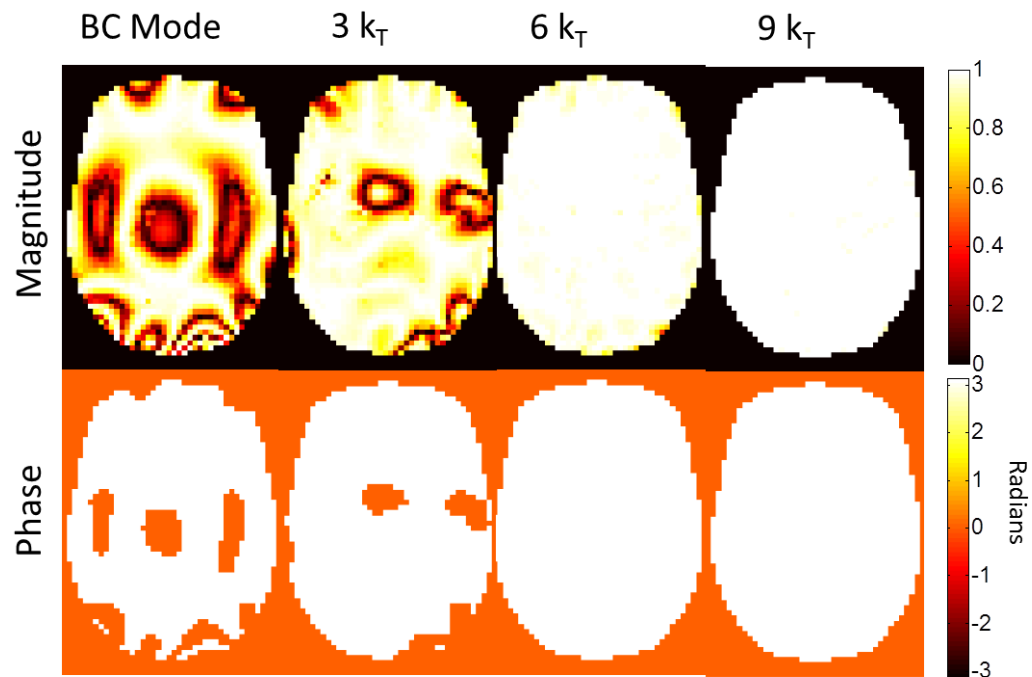


Figure 15: The comparison between circularly polarized birdcage mode, RF shimming (1  $k_T$ -point), 3  $k_T$ -points, 6  $k_T$ -points and 9  $k_T$ -points cases at large tip angle using the full Bloch simulation method with a least squares algorithm. Target tip angle:  $90^\circ$  (target magnetization: 1), target phase: flat  $0^\circ$ .

Table 2: The peak RF voltage, peak 10g local SAR and global SAR values of the pulses in Figure 15. A duty cycle of 10% was assumed.

	BC Mode	RF Shimming	3 $k_T$	6 $k_T$	9 $k_T$
Peak RF (V)	316	460	531	437	427
Peak 10g LSAR (W/kg)	30	45.5	24.4	9.8	3.5
GSAR (W/kg)	5.7	6.6	2.6	1.1	0.6



RMSE z:	66%	47%	2%	0.5%
Mag z mean	-0.57	-0.77	-0.98	-0.999
Phase z mean (°)	151.6	165.9	171.9	180
Norm Mag z Std (%)	86.6	52.9	3.1	0.4
Phase z Std (°)	65.6	48.4	0	0
Dev z 10% (%)	0	63	98	100
Dev z 20% (%)	0	76	99.5	100
Duration (ms)	0.5	1.77	3.53	5.29

Figure 16: The comparison between circularly polarized birdcage mode, RF shimming (1  $k_T$ -point), 3  $k_T$ -points, 6  $k_T$ -points and 9  $k_T$ -points cases at large tip angle using the full Bloch simulation method with a least squares algorithm. Target tip angle: 180° (target magnetization: 1), target phase: flat 0°.

Table 3: The peak RF voltage, peak 10g local SAR and global SAR values of the pulses in Figure 16. A duty cycle of 10% was assumed.

	BC Mode	3 kt	6 kt	9kt
Peak RF (V)	633	1636	964	508
Peak 10g LSAR (W/kg)	121.7	164.7	34.3	15.8
GSAR (W/kg)	23	17	5.1	2

## 4.2 Least Squares vs Magnitude Least Squares

As discussed in the Background section, many of the MRI applications require a flat magnitude excitation profile whereas the phase profile does not matter. The phase target puts extra burden on the pulse design algorithm which results in a worse magnitude profile than the case with relaxed phase constraints. As shown in the Background and the Methods sections, it is possible to implement a magnitude least squares version of both the STA approximation method and the full Bloch method. In this section, the least squares and the magnitude least squares versions of both algorithms are compared for small and large tip angle cases.

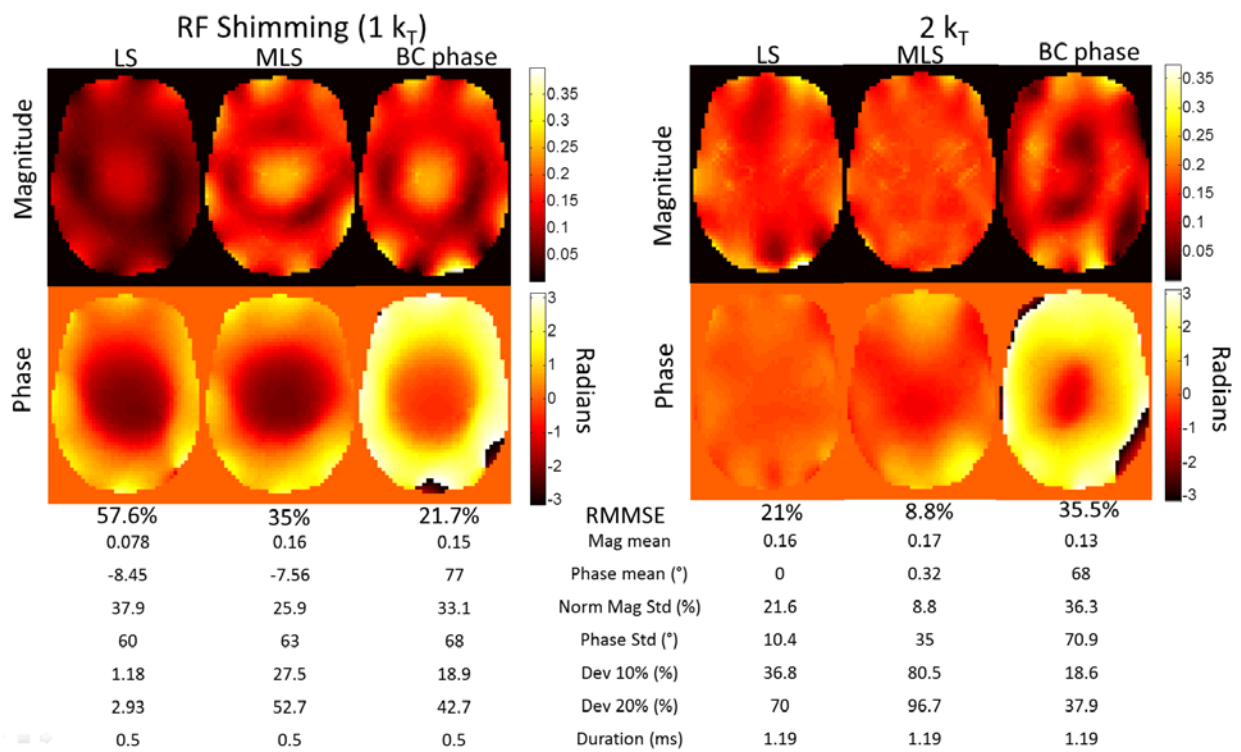


Figure 17: The comparison of the least squares (LS), magnitude least squares (MLS) and the least squares algorithm with the BC mode phase target (BC phase) for 1 and 2  $k_T$ -points. Target flip angle:  $10^\circ$ , target phase: flat  $0^\circ$  for LS and MLS, volume of interest: a slice of thickness 4mm.

Additionally, noticing that the phase profile of the RF shimming case looks very similar to the phase profile of the BC mode except a possible constant phase shift, the BC mode phase can be given as the phase target to the least squares algorithm with the expectation to imitate the magnitude least squares algorithm. In fact as expected, the least squares algorithm performs poorly for 1  $k_T$ -point, the excitation profile improves drastically when magnitude least squares is used and using the BC mode phase as the target phase for the least squares algorithm results in an excitation fidelity between that of

the LS and the MLS algorithms. This is observed both for small ( $10^\circ$ ) and large tip angle ( $90^\circ$ ) pulses. (Figure 17 and Figure 18) Moving to 2  $k_T$ -points, the MLS algorithm still outperforms the LS algorithm whereas the BC mode phase as the target phase no longer improves the excitation fidelity of the LS algorithm but actually deteriorates it (Figure 17, Figure 18).

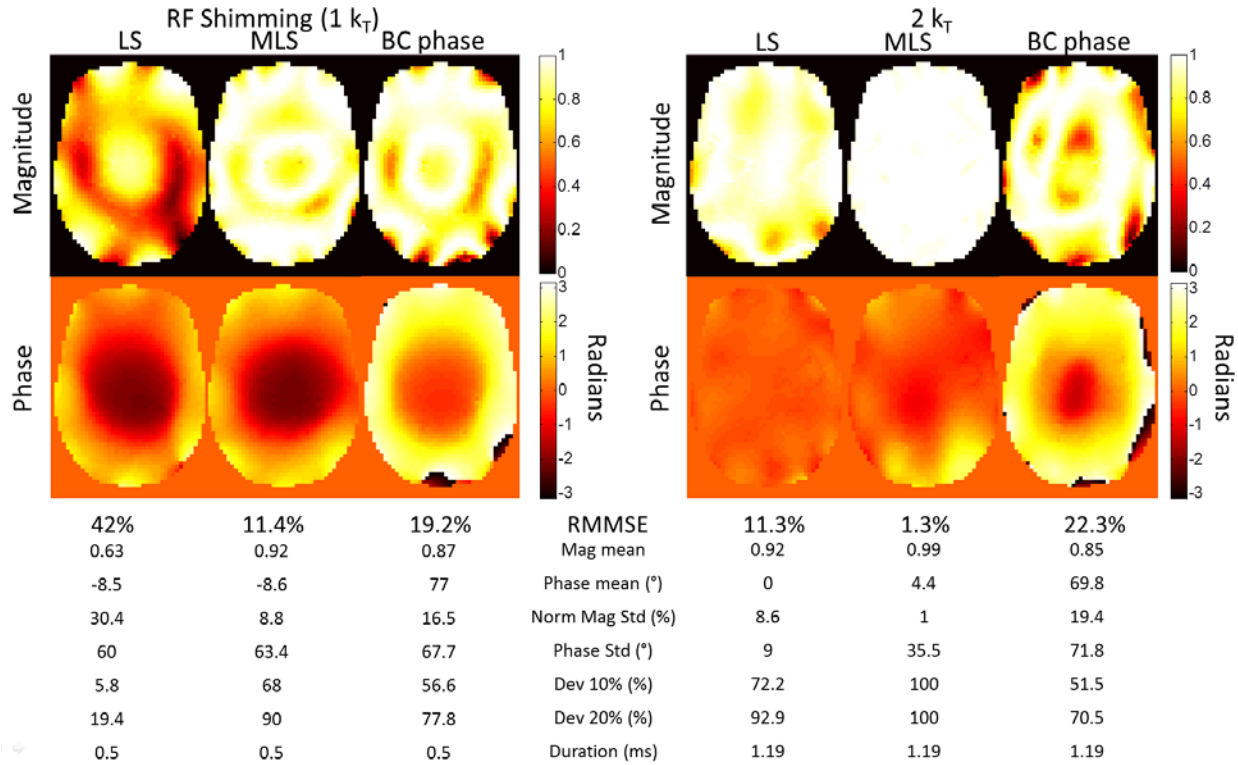


Figure 18: The comparison of the least squares (LS), magnitude least squares (MLS) and the least squares algorithm with the BC mode phase target (BC phase) for 1 and 2  $k_T$ -points. Target flip angle:  $90^\circ$ , target phase: flat  $0^\circ$  for LS and MLS, volume of interest: a slice of thickness 4mm.

To sum up, the MLS approach immensely improves the magnitude profile of the RF pulse but at the cost of a longer design time (optimization duration). Using the BC mode phase as the target phase of an LS algorithm results in an excitation profile close to that of an MLS algorithm with the design time of an LS algorithm. However, this approach works only for 1 $k_T$ -point. Consequently, the optimal phase target for the LS algorithm that will imitate the MLS algorithm for more general cases than the RF shimming case remains an open problem.



### 4.3 Constrained Pulse Design

All pulse designs until now have been unconstrained in the sense that the peak RF voltage, peak local SAR and global SAR values were allowed to be as high as the pulse algorithm required to achieve a good excitation fidelity. However, there are hardware and safety limits on these values and it is important to optimize an RF pulse subject to these limits especially at large tip angles where these limits are even more restricting. In this section, the RF and SAR constraints are added to the full Bloch simulation method and the performance of the full Bloch simulation method is analyzed for several different constraints.

#### 4.3.1 Effects of Constraints on Excitation Profile

To demonstrate the effect of constraints on the excitation profile, one example constraint (a maximum RF voltage value of 30 V) for both small and large tip angle cases are introduced and the resulting excitation profiles are compared with their corresponding unconstrained cases. The RF peak voltage constraint severely punishes both the STA and the LTA pulses but the effect is clearly more substantial for the 90° excitation case (Figure 19).

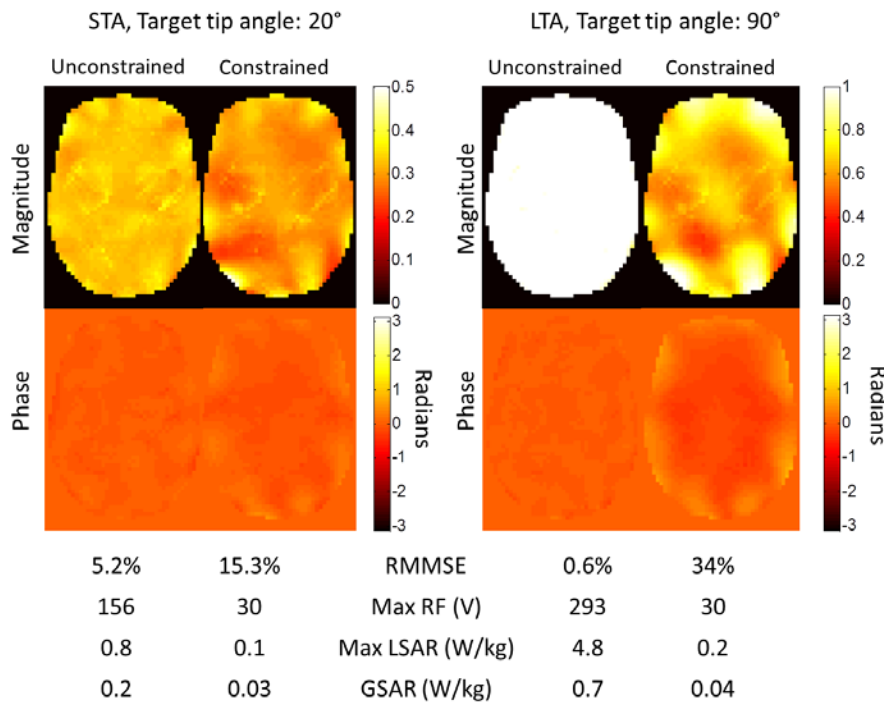


Figure 19: Comparison of the performances of an unconstrained RF pulse and a constrained RF pulse at small tip angle (20° target tip angle, 5  $k_T$ -points) and large tip angle (90° target tip angle, 5  $k_T$ -points) regimes. The constraint is a maximum RF voltage value of 30 V for both cases.

### 4.3.2 L-Curves

The novelty of the full Bloch simulation method lies in the fact that it can control local SAR and global SAR explicitly as well as RF peak voltage as opposed to only RF peak voltage. When compared to the case where SAR is limited by limiting the peak RF voltage, constraining SAR explicitly in the design algorithm is expected to result in more optimal pulses. In this section, the performances of peak RF voltage, peak 10g LSAR and GSAR constrained pulse designs are compared using L-curves. The L-curves for each three cases are produced by varying one limit while keeping the other two constant. (e.g. the LSAR L-curve is produced by varying the peak 10g LSAR limit while keeping the GSAR and peak RF voltage limits constant). Then the peak 10g local SAR, global SAR and peak RF voltage values of all three designs are plotted and compared for excitation, inversion and refocusing pulses. For all designs a duty cycle of 10% was assumed when calculating SAR.

Figure 20 shows the resulting peak LSAR values of LSAR, GSAR and RF voltage constrained designs for various limits. It can be observed that for the same 10g peak LSAR value, the LSAR constrained design has lower excitation error than the RF voltage constrained design. For a visual representation of an example design point (the point on the LSAR constrained curve with an RMMSE of 2 % and peak 10g LSAR value of 1.2 W/kg) on Figure 20 see Figure 21.

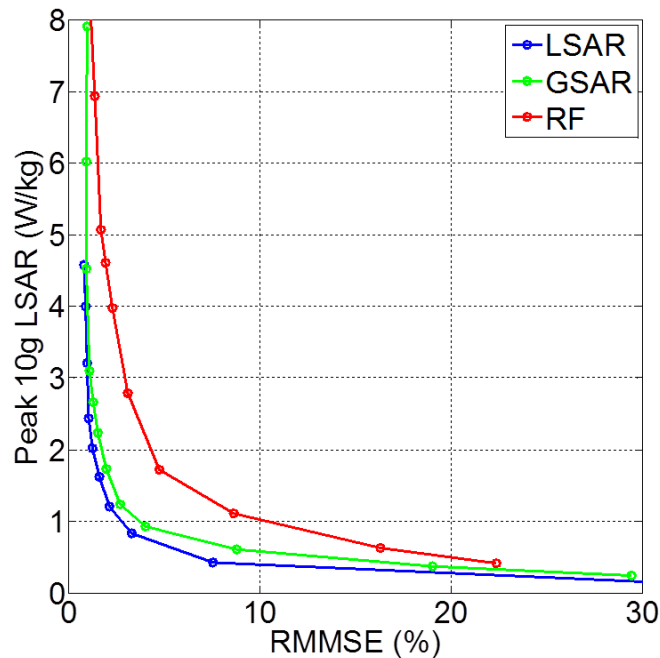


Figure 20: The comparison of peak 10g LSAR, GSAR and peak RF voltage constrained designs using 9  $k_T$ -points. Target tip angle:  $90^\circ$ , target phase: flat  $0^\circ$ .

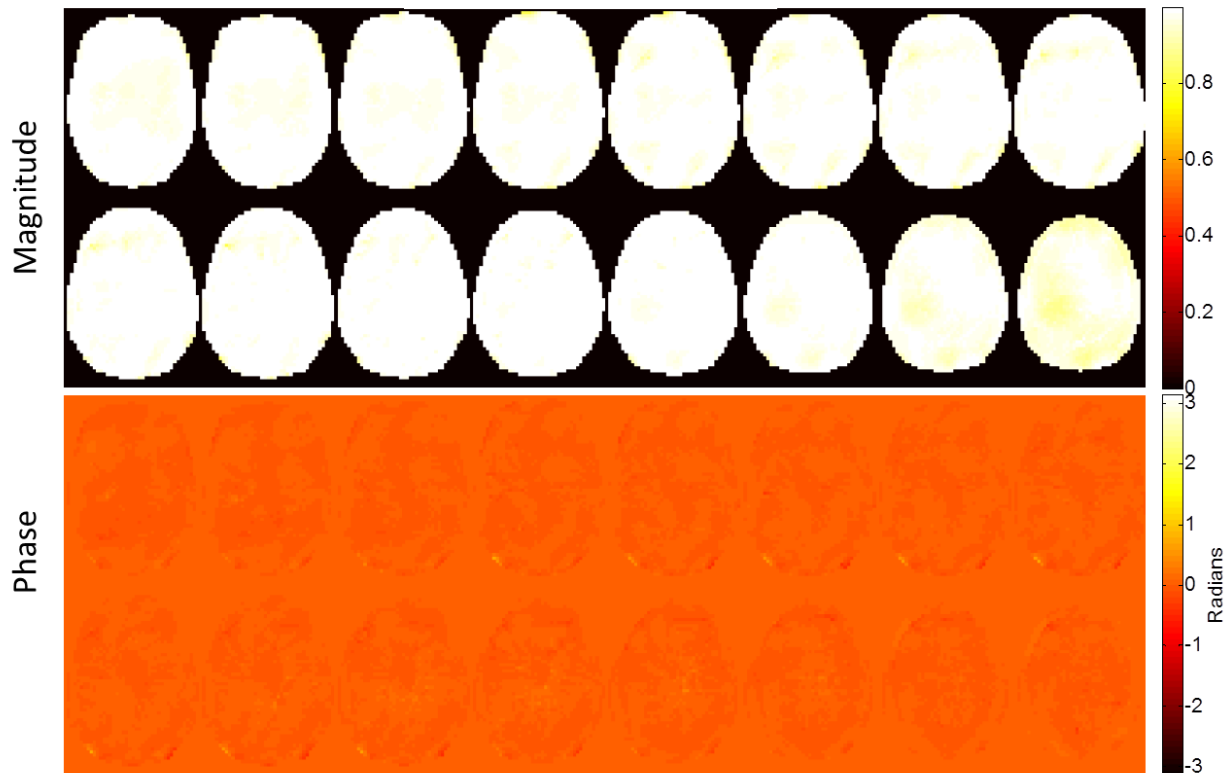


Figure 21: The magnitude and phase of the resulting magnetization for all 16 slices of a point near the elbow of the LSAR constrained (blue) L-curve in Figure 20 with an RMMSE of 2 % and peak 10g LSAR of 1.2 W/kg. Design time: 60 s for LCLTA, 280 s for full Bloch simulation method.

Looking at the GSAR and the peak RF voltage values of the same L-curves in Figure 20, the reason why the LSAR constrained curve is closer to the origin than the RF voltage constrained curve can be explained more easily (Figure 22). For the same excitation fidelity, the LSAR constrained curve has a lower 10g peak LSAR value than the RF constrained curve while its peak RF voltage value is higher. This means, the LSAR constrained design can lower the peak 10g LSAR value without having to lower the peak RF voltage value. This is in fact the expected behavior of an explicitly SAR constrained design because the peak RF voltage value and the peak 10g LSAR value are not linearly related. On the other hand, the RF constrained design has to lower its peak RF voltage value to lower the resulting peak 10g LSAR value. Therefore, the LSAR constrained design has more degrees of freedom than the RF constrained design and hence is able to achieve better excitation profiles.

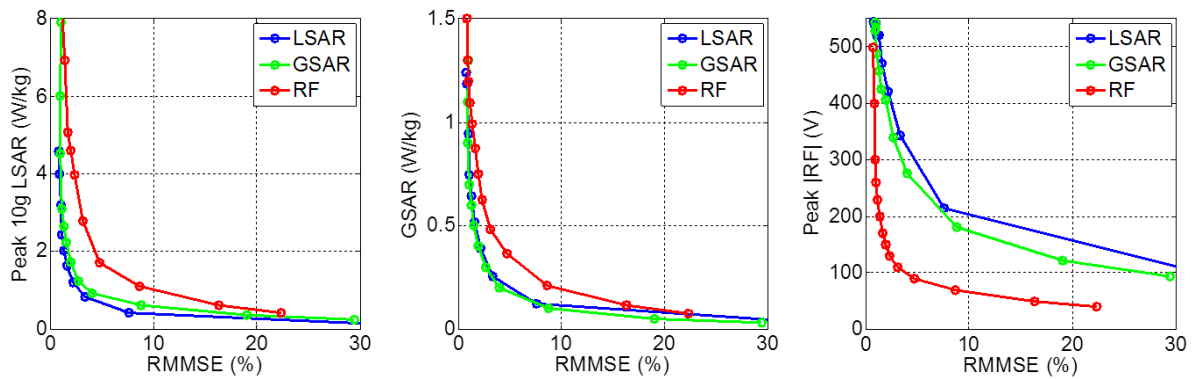


Figure 22: Peak 10g LSAR, GSAR and peak RF voltage values of the three designs in Figure 20.

The RF peak voltages of the designs in Figure 22 get as high as 500 V whereas the hardware limit for most MRI systems currently are at or below 200 V. In Figure 22, when producing one L-curve the other two limits have been chosen so high that practically those two quantities are unconstrained. If the same comparison is to be made with all practical limits then we can keep all three limits at or below the hardware and safety limits at all times. The FDA safety limits for 10g peak LSAR and GSAR at head are 8 W/kg and 3 W/kg respectively (27) and the hardware limit for peak RF voltage has been chosen as 200 V. The L-curves in Figure 23 are produced in the same way as in Figure 22 but with these 3 practical limits as the maximum allowable limits for peak 10g LSAR, GSAR and peak RF voltage at all times. The L-curve patterns are very similar to Figure 22 except the RF peak value curves. Notice that the LSAR and GSAR constrained curves use all available RF peak voltage for most of the cases while lowering SAR whereas for the same RF peak voltage value (200 V) the RF constrained design has a much higher SAR value.

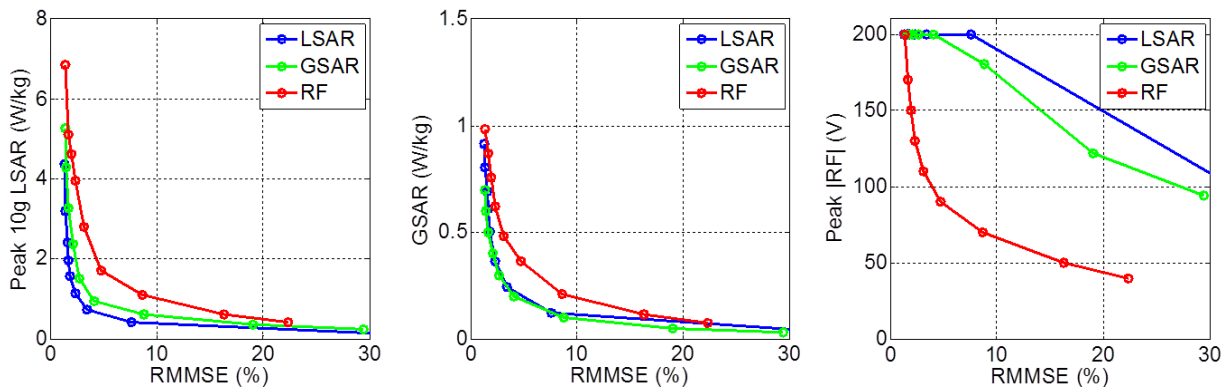


Figure 23: The comparison of peak 10g LSAR, GSAR and peak RF voltage constrained designs using 9  $k_T$ -points. Target tip angle:  $90^\circ$ , target phase: flat  $0^\circ$ . For all designs not exceeding the practical limits of 8 W/kg peak 10g LSAR, 3 W/kg GSAR and 200 V peak RF voltage was ensured.

The 1 limit at a time (only one of LSAR, GSAR or RF is limited for each individual L-curve) and the 3 limits at a time (all of LSAR, GSAR and RF values are limited for each individual L-curve while only one is being varied throughout the L-curve) cases are compared in Figure 24. Allowing the RF peak voltage value to be as high as the pulse requires results in improved excitation fidelity for the LSAR and GSAR constrained designs while for the RF constrained design the two cases overlap until the hardware limit. This implies that the designs are more limited by the peak RF voltage than they are by the peak 10g LSAR or GSAR.

For the rest of this section, the effect of some design parameters such as the optimizing algorithm (LS or MLS) and the number of  $k_T$ -points on the L-curves are analyzed. Also noticing that some of the points on the L-curves take several hours to be optimized by the algorithm, a few approaches in making the process faster are taken such as down sampling the  $B_1^+$  field maps or changing the tolerance of the optimizing algorithm and the influence of these changes on the excitation fidelity performance of the full Bloch simulation method is analyzed.

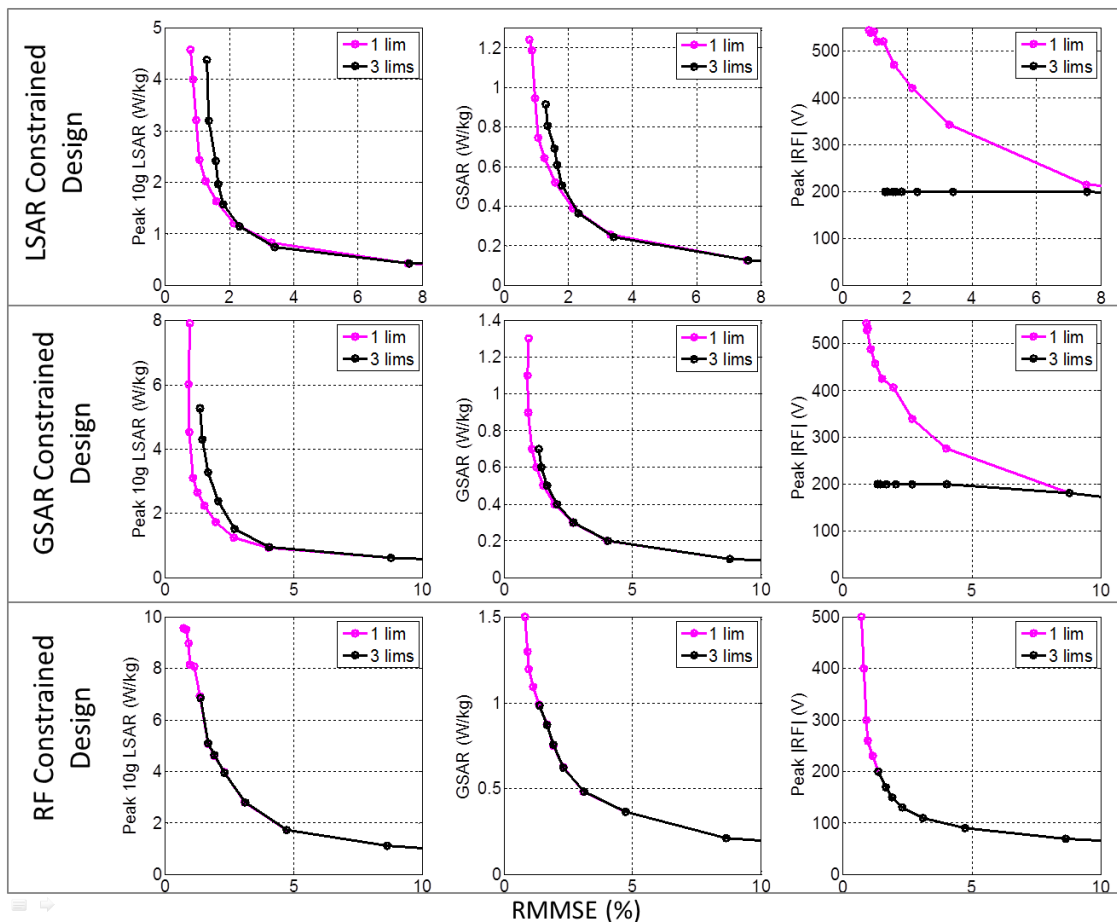


Figure 24: Comparison of the 10g LSAR, GSAR and peak RF voltage values of the 3 curves (blue, green and red) in Figure 22 and Figure 23.

### 4.3.2.1 Optimizing Algorithm

The same set of L-curves in Figure 23 are produced using a magnitude least squares algorithm for all RF pulses in Figure 25 to compare the least squares and the magnitude least squares algorithm results. A very similar pattern is observed for both cases except that the excitation fidelity is much better as well as the pulse design takes much longer for the MLS designs.

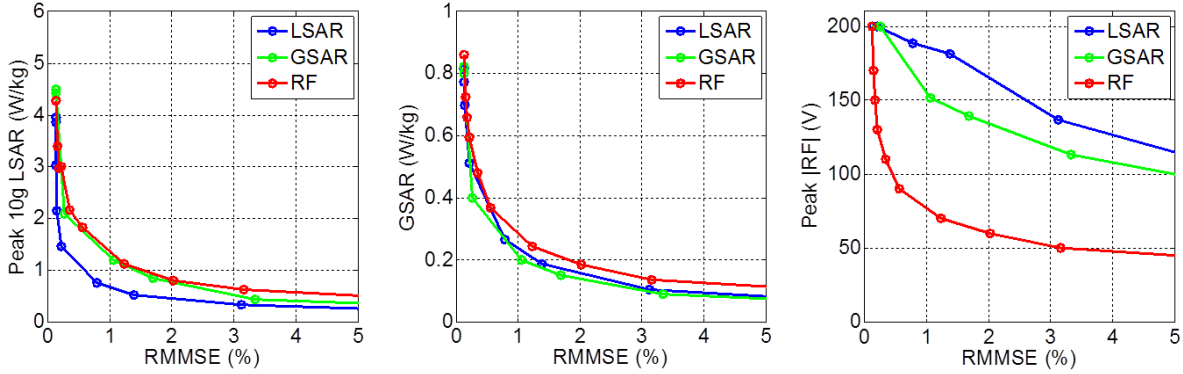


Figure 25: The comparison of peak 10g LSAR, GSAR and peak RF voltage constrained designs using 9  $k_T$ -points and a magnitude least squares algorithm. Target tip angle:  $90^\circ$ .

### 4.3.2.2 Number of $k_T$ -points

As the number of  $k_T$ -points increase from 6  $k_T$ -points up to 12  $k_T$ -points, the structure of the three sets of plots stay the same while the excitation error gets lower as expected (Figure 26).

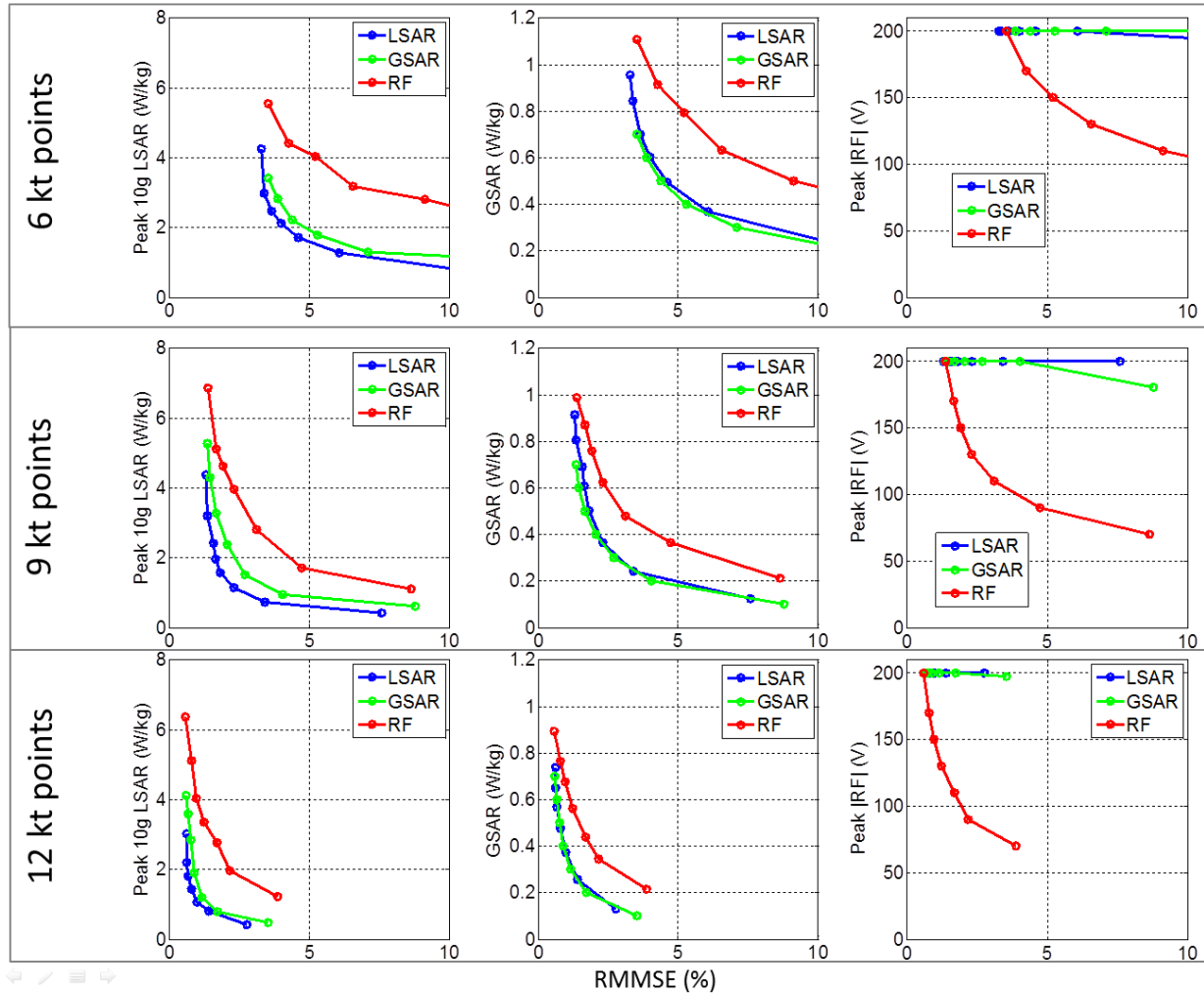


Figure 26: The comparison of peak 10g LSAR, GSAR and peak RF voltage constrained designs using 6  $k_T$ , 9  $k_T$  and 12  $k_T$  points with a least squares algorithm. Target tip angle:  $90^\circ$ , target phase:  $0^\circ$ .

#### 4.3.2.3 Down sampling the $B_1^+$ Maps

The resolution of the transmit field maps is 4 mm isotropic. The field maps are down sampled by a factor of 1 (no down sampling) and 3 (1.2 cm) isotropically and the L-curves are produced for the two cases (Figure 27). The design times for both down sampling rates can be found in Figure 28. It is possible to conclude that, down sampling the  $B_1^+$  maps *for this configuration* by a factor of 3 does not affect the pulse design algorithms performance while making it faster hence is profitable.

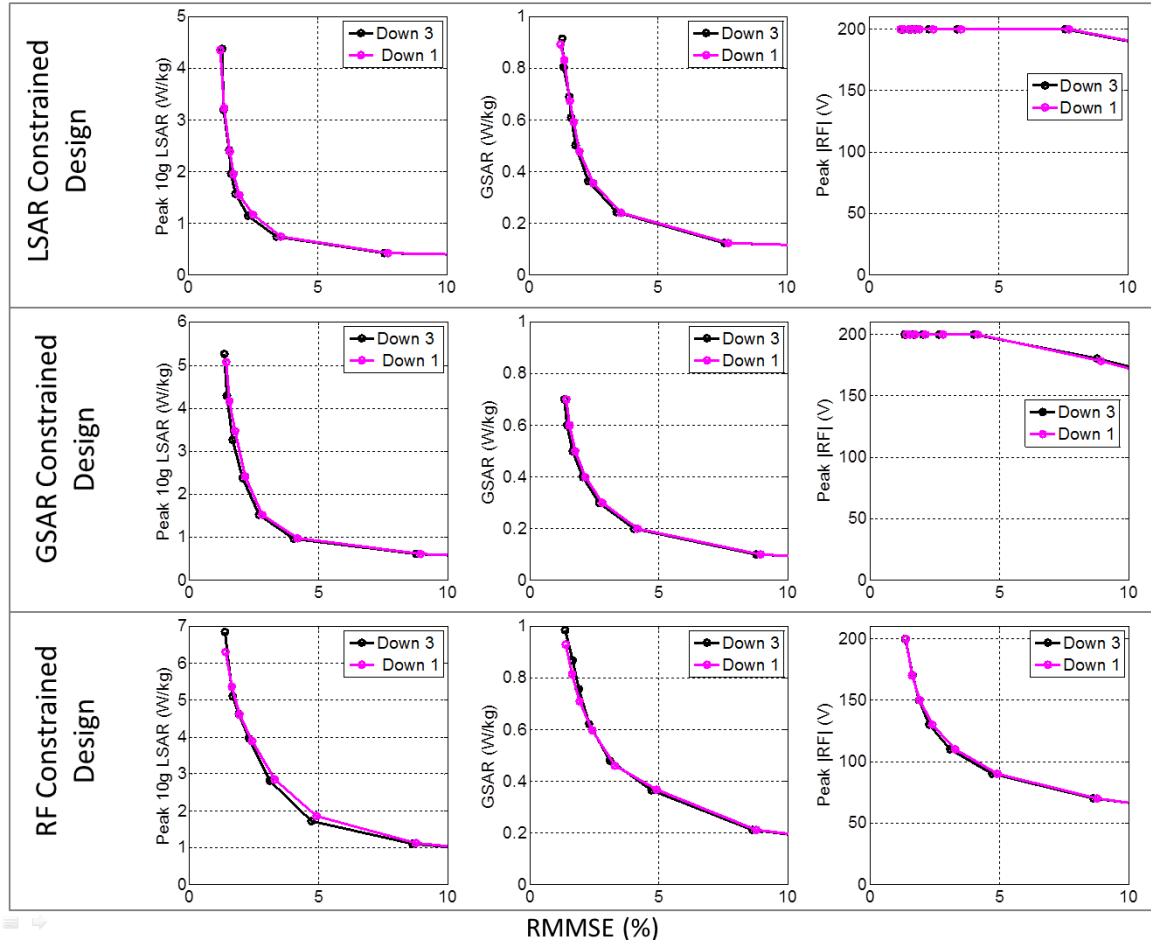


Figure 27: Effect of down sampling the transmit field maps on the performance of LSAR, GSAR and RF constrained designs. Target tip angle:  $90^\circ$ , target phase: flat  $0^\circ$ , number of  $k_T$ -points: 9, algorithm: least squares

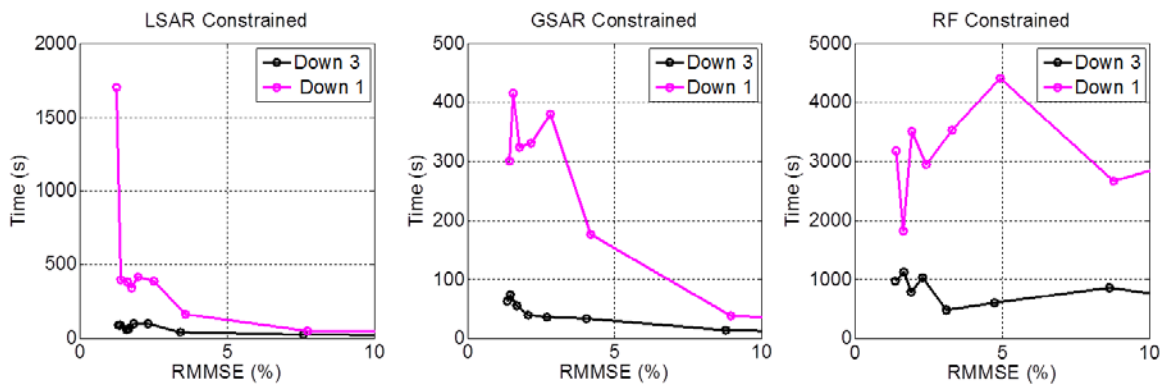


Figure 28: The comparison of the speed of the two algorithms with different down sampling rates for the transmit field maps for all three designs (LSAR, GSAR and RF constrained) in Figure 27.



### 4.3.2.4 Tolerance of the Optimizing Algorithm

To speed up the pulse design algorithm, another option is to decrease the tolerance of the optimizing algorithm without changing its performance. Figure 29 shows the comparison of the performances of the full Bloch simulation method for two tolerance values,  $10^{-6}$  and  $10^{-3}$  while Figure 30 shows their speed. Similarly to the transmit field down sampling case, *for this configuration* it is profitable to decrease the tolerance of the optimizing algorithm.

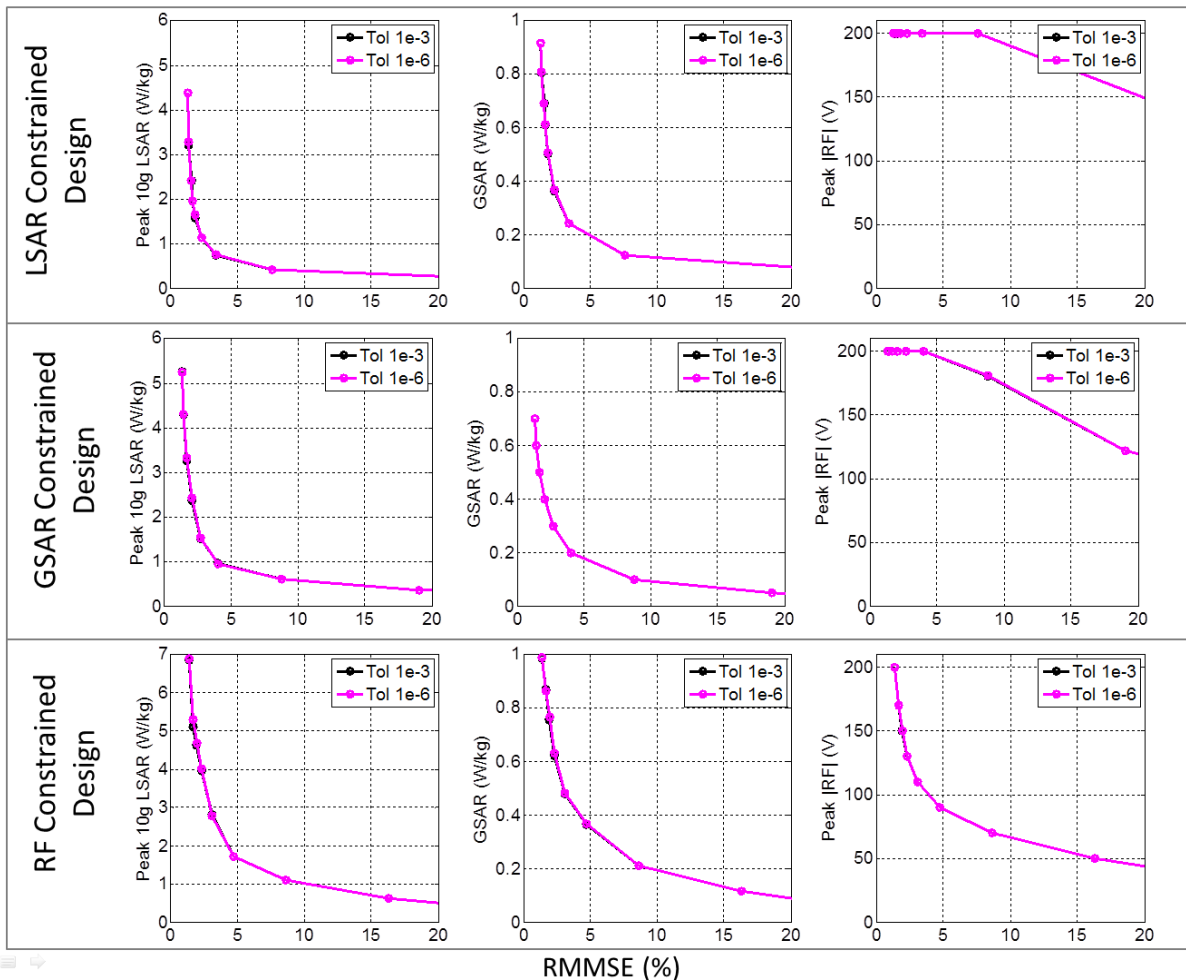


Figure 29: Effect of the tolerance value of the optimizing algorithm on the performance of LSAR, GSAR and RF constrained designs. Target tip angle:  $90^\circ$ , target phase: flat  $0^\circ$ , number of  $k_T$ -points: 9, algorithm: least squares.

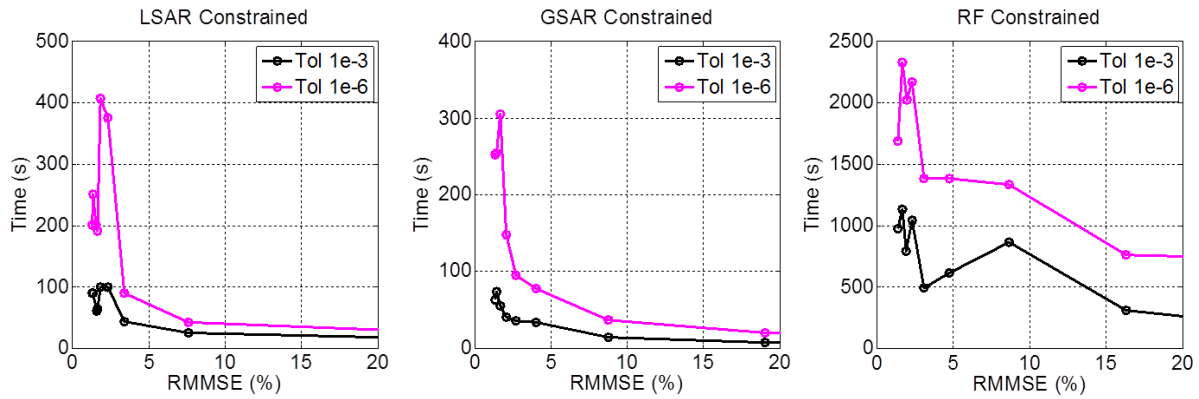


Figure 30: The comparison of the speed performance of the two algorithms with different tolerance values for the optimizing algorithm in Figure 29.

#### 4.3.2.5 Inversion Pulses

The L-curve analysis approach for  $90^\circ$  excitation pulses is extended to  $180^\circ$  inversion pulses in this section. Since these two classes of pulses are designed in the same way except a tip angle difference, the parameter analysis (number of  $k_T$ -points, down sampling rate, tolerance) is not repeated here. Notice that for the same excitation fidelity, the  $180^\circ$  pulses for all designs in Figure 31 have larger SAR and RF voltage values than the  $90^\circ$  pulses in Figure 23. This is because in order to tip spins by a larger amount (larger tip angle) one needs to deposit more RF energy (higher RF voltage and SAR). For a visual representation of the inversion pulse design performances a point on the LSAR constrained (blue) curve in Figure 31 is chosen (the point near the elbow with an RMMSE of 6 % and peak 10g LSAR of 2 W/kg) and its magnitude and phase profiles are plotted in Figure 32.

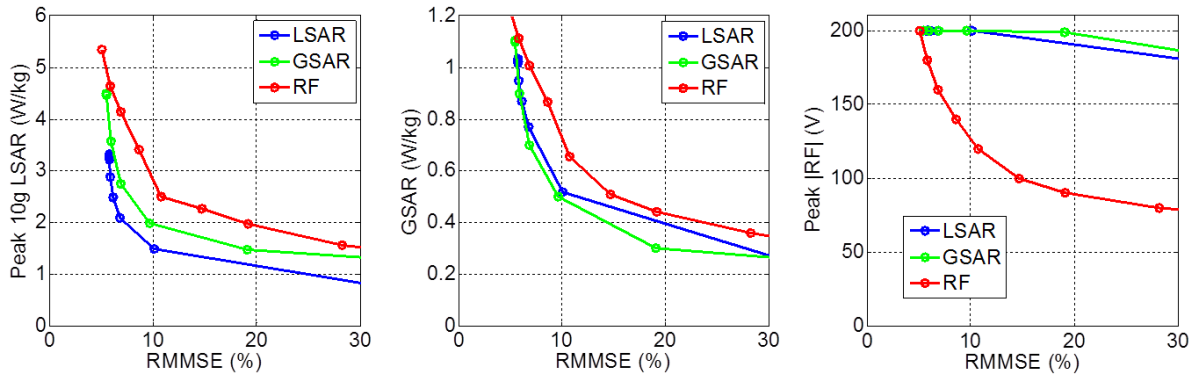


Figure 31: The comparison of peak 10g LSAR, GSAR and RF peak voltage constrained inversion RF pulse designs using 9  $k_T$ -points and a least squares algorithm. Target tip angle:  $180^\circ$

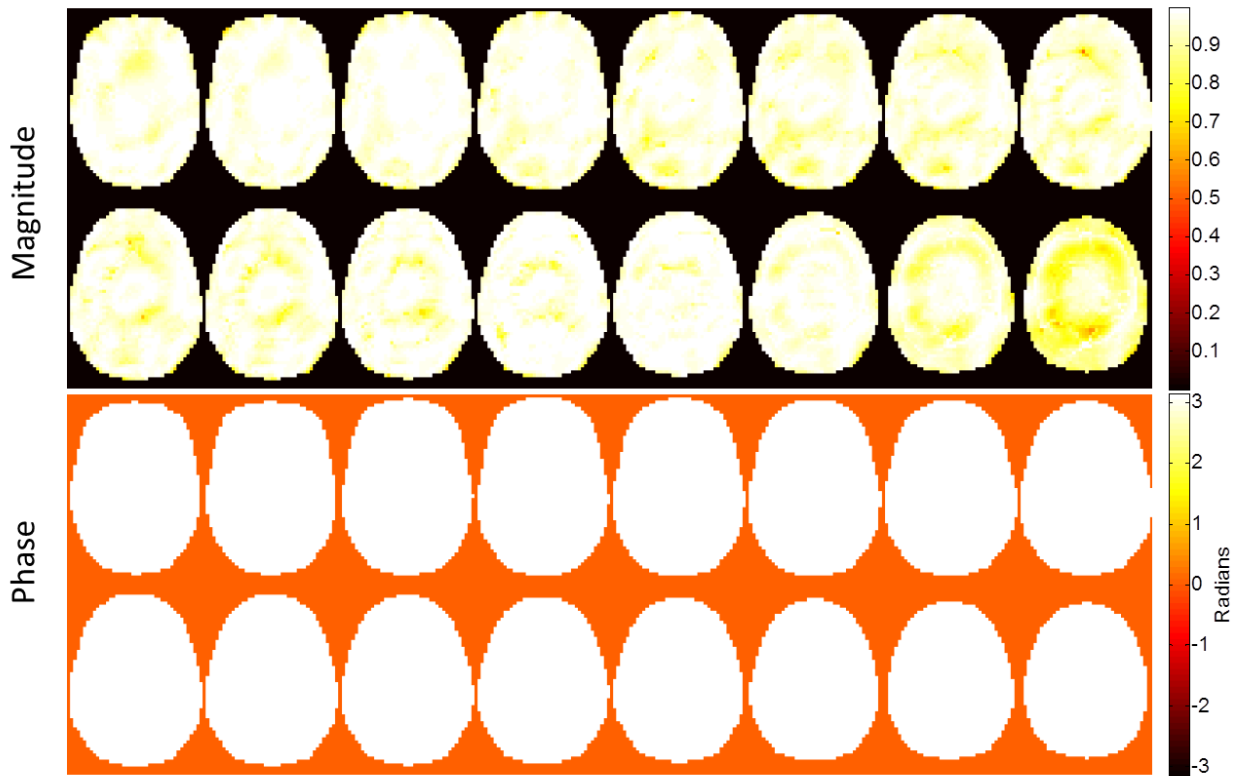


Figure 32: The magnitude and phase of the resulting magnetization for all 16 slices of a point near the elbow of the LSAR constrained (blue) L-curve in Figure 31 with an RMMSE of 6 % and peak 10g LSAR of 2 W/kg. Design time: 47 s for LCLTA, 2131 s for full Bloch simulation method.

### 4.3.2.6 Refocusing Pulses

The L-curve analysis approach for  $90^\circ$  excitation pulses is extended to  $180^\circ$  refocusing pulses in this section. Since in simulation the effect of the crusher gradients cannot be realized, the RMMSE in Figure 32 refers to the error in the designed  $\beta$  in Equation (3.26). When these RF pulses are combined with crusher gradients, in the ideal case (perfect crusher gradients, no  $B_0$  inhomogeneities, etc.) the RMMSE of the magnetization profile should be the same as of the RMMSE of  $\beta$ . Also, the refocusing pulses in this section are designed for a rotation axis along the x-axis ( $0^\circ$  target phase for  $\beta$ ). For a visual representation of the refocusing pulse design performances a point on the LSAR constrained (blue) curve in Figure 33 is chosen (the point near the elbow with an RMMSE of 8 % and peak 10g LSAR of 2.5 W/kg) and its magnitude and phase profiles are plotted in Figure 34.

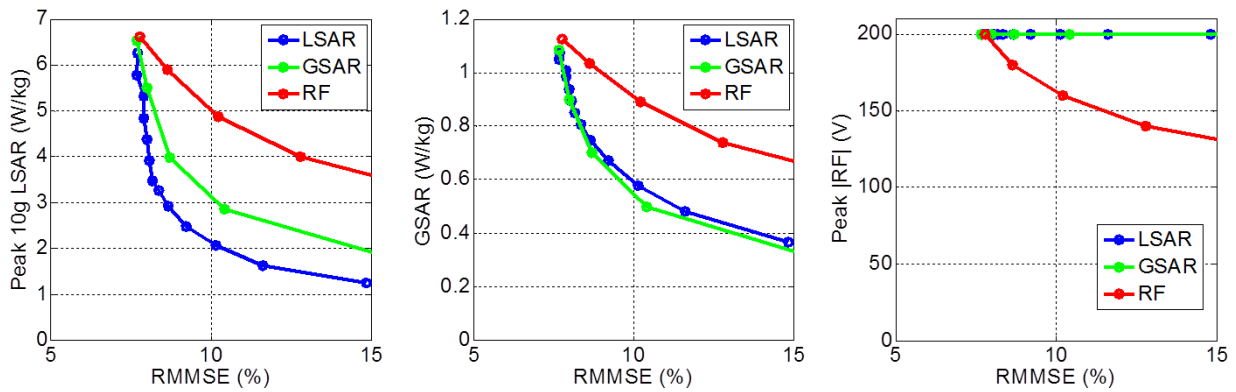


Figure 33: The comparison of peak 10g LSAR, GSAR and RF peak voltage constrained refocusing RF pulse designs using 12  $k_T$ -points and a least squares algorithm. Target tip angle:  $180^\circ$ , target phase: flat  $0^\circ$  (i.e. rotation axis for the spins: x-axis)

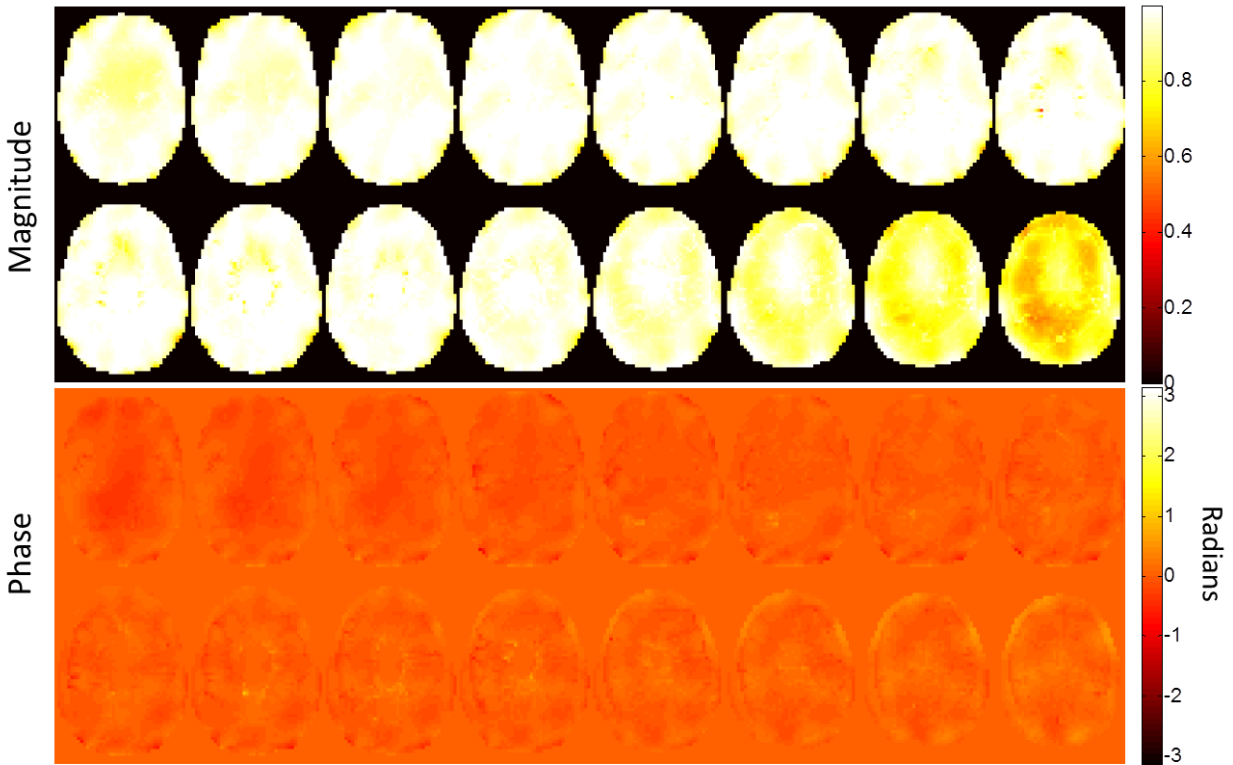


Figure 34: The magnitude and phase of the  $\beta$  (the target for the refocusing pulse design, Equation (3.26)) for all 16 slices of a point near the elbow of the LSAR constrained (blue) L-curve in Figure 33 with an RMMSE of 8 % and peak 10g LSAR of 2.5 W/kg. Design time: 76 s for LCLTA, 2080 s for full Bloch simulation method.

## 5 Conclusion, Discussion and Future Work

In this thesis an explicitly SAR constrained large tip angle pulse design algorithm to mitigate the transmit field inhomogeneities at high field systems was developed and analyzed.

First, the significance of RF excitation pulse design at small tip angle (STA) domain was demonstrated by comparing the excitation profiles of circularly polarized birdcage mode, RF shimming (1  $k_T$ -points) and several  $k_T$ -points pulses for the unconstrained case (no LSAR, GSAR or peak RF voltage constraints). This was done for the purposes of comparison with the large tip angle (LTA) case in order to have a more comprehensive understanding of the developed method as well as to build confidence in it.

Second, the need for a large tip angle pulse design algorithm was demonstrated by showing the poor performance of the small tip angle approximation and linear class of large tip angle (LCLTA) pulses methods at large tip angles. Then the excitation fidelities for all target tip angles between  $10^\circ$  and  $180^\circ$  of RF pulses designed with the full Bloch simulation method were plotted. It was found out that even for the unconstrained case the RF pulses designed for target tip angles of  $170^\circ$  and  $180^\circ$  were not able to achieve the targeted mean. On the other hand, for tip angles below  $170^\circ$  the excitation fidelities were almost perfect and moving from  $160^\circ$  to  $170^\circ$  target tip angle there was a sudden drop in the excitation fidelity. Moreover the standard deviations of the RF pulses for tip angles  $170^\circ$  and  $180^\circ$  were almost zero. Hence the designed profiles were perfectly homogeneous with means lower than the target. These imply that the imperfect excitation profiles at  $170^\circ$  and  $180^\circ$  tip angles are most probably due to a bad initial point determined by the LCLTA method. Nevertheless, the initial point is a part of the algorithm and needs to be paid special attention at all times as it plays a vital role in the excitation profile of the finalized RF pulse.

Third, the significance of RF excitation pulse design at large tip angle domain was demonstrated by comparing the excitation profiles of circularly polarized birdcage mode, RF shimming (1  $k_T$ -points) and several  $k_T$ -points pulses again for the unconstrained case. It was observed that the STA approximation and full Bloch simulation methods are both severely limited by the target phase restriction which in most applications in MRI is irrelevant as long as the phase variation across a voxel is small enough. It was also worth noting that the excitation error of the full Bloch simulation method for a target tip angle of  $90^\circ$  was smaller than the excitation error of the STA approximation method for a target tip angle of  $10^\circ$  for the same RF pulse duration and same  $k$ -space trajectory. This feature of the full Bloch simulation method comes at the cost of a longer pulse design duration. Furthermore, the resulting peak RF voltage, GSAR and peak 10g LSAR values of the designs at large tip angles were much higher than those at small tip angles as expected.

In an attempt to improve the magnitude profile of the RF pulses by relaxing the phase constraint, the magnitude least squares (MLS) algorithm was implemented both for the STA

approximation and the full Bloch simulation methods. When compared to the conventional least squares (LS) approach, the MLS algorithm improved the magnitude profile drastically at the cost of a longer pulse design duration. In order to combine the short pulse design duration feature of the LS algorithm with the improved magnitude profile of the MLS algorithm, a CP BC mode phase was used as the target phase of an LS algorithm which resulted in an excitation profile between that of an LS and an MLS algorithm. Nevertheless, this approach worked profitably only for the 1  $k_T$ -point case. For higher number of  $k_T$ -points a simple/fast to obtain target phase profile that can improve the magnitude profile of an LS algorithm remains as an open question.

The analysis summarized above was carried out to evaluate the capabilities of the full Bloch simulation hence the RF pulses designed were unconstrained. Transitioning from the unconstrained case to the constrained case, it was verified that the RF and SAR constraints are much more restrictive for large tip angle pulses than they are for small tip angle pulses. This is only expected since previously it was found out that the resulting RF and SAR values of the unconstrained LTA pulses were much higher than those of the unconstrained STA pulses.

Comparing the peak 10g LSAR, GSAR and peak RF voltage constrained designs using L-curves, it was observed that the LSAR curve is closer to the origin than the RF curve. This was explained by the fact that most of the points on the LSAR curve make use of all of the peak RF voltage available and yet minimize SAR while the RF curve had to decrease the peak RF voltage of the pulse to minimize SAR. Comparing the case where only one quantity is limited at a time with the case where all three quantities are limited (so that all the limits are at or under the safety and hardware limits), it was noted that for the same SAR limits allowing more RF voltage improved the performance of the pulse whereas for the same RF limit allowing more LSAR and GSAR did not change the result. This indicates that peak RF voltage is a more restrictive limit than the SAR limits and constraining SAR via limiting the peak RF voltage is not the optimal approach.

Using an MLS algorithm instead of an LS algorithm, a similar set of L-curves were obtained with the difference that they are closer to the origin due to the superior performance of the MLS algorithm. As previously discussed, the MLS approach converts the problem from convex to non-convex for the STA approximation and the LCLTA method. For the full Bloch simulation method, the problem is already non-convex so the MLS approach adds another layer of non-convexity to the problem, making the initial point even more crucial.

As expected, as the number of  $k_T$ -points in the k-space trajectory was increased, the relative positions of the three L-curves remained the same while the overall excitation error dropped. Then, the tradeoff is between the excitation fidelity and the design time since the pulse design duration increases with increasing number of  $k_T$ -points.

Noticing that the pulse design duration of some of the less constrained points on the L-curves with lower excitation errors went up to a few hours, down-sampling the transmit field maps and increasing the tolerance of the optimization algorithm were proposed. It was concluded that these are valid approaches in making the algorithm faster without altering its performance for certain

configurations. However, for every alteration of the configuration (different number of  $k_T$ -points, excitation/inversion/refocusing pulses) the effect of these tricks on the L-curves must be seen before they are adopted due to the non-convexity of the problem in hand.

All of the above constrained RF pulse design analysis was for excitation pulses with a target tip angle of  $90^\circ$ . The approach is easily extended to inversion and refocusing pulses. The effect of this transition was higher peak 10g LSAR, GSAR and peak RF voltage values for the same excitation error when compared to the excitation case. The L-curves are the closest to the origin for the  $90^\circ$  excitation case whereas they are furthest for the case of refocusing pulses. This is expected since as the tip angle increases or the RF pulse becomes more desiring (refocusing pulse) the excitation error increases for the same set of constraints. Not only the L-curves are further away from the origin but also the relative positions of the LSAR, GSAR and RF L-curves for the inversion and refocusing pulses depend much more dramatically on the initial point. This is because the LCLTA algorithm performs well at  $90^\circ$  but poorly for  $180^\circ$  hence it is much more probable for an inversion or refocusing pulse to have higher than expected excitation error due to a bad initial point.

A more general look on the L-curves produced reveal that all three L-curves (LSAR, GSAR and RF constrained) converge to the same point or head towards it for the case of 8W/kg peak 10g LSAR, 3 W/kg GSAR (safety limits) and 200V peak RF voltage (hardware limit). In other words, for the same limits the three L-curves have the same excitation error. This possibly means that the three L-curves are in the neighborhood of the same local minimum if not the global minimum and it is fair to compare their performances. Cases where top points (the point for which the peak 10g LSAR limit is 8W/kg GSAR limit is 3W/kg and peak RF voltage limit is 200 V) of the three L-curves do not converge to the same point have occurred and in that case it should be known that the L-curve whose top point has higher excitation error is definitely around a local minimum but not the global minimum and there is room for improvement at least until its top point reaches the excitation error of the other L-curves' top points.

Future work includes:

- Further analysis and possible improvement of the initial point of the full Bloch simulation algorithm determined by the LCLTA algorithm
- MLS, number of  $k_T$ -points, down-sampling the transmit field and changing the optimization tolerance analysis for inversion and refocusing pulses
- Spectral profile analysis of  $90^\circ$  excitation, inversion and refocusing pulses
- Main field ( $B_0$ ) inhomogeneity incorporation into the pulse design algorithm and experimental verification of it on a high field MRI scanner
- Joint optimization of the k-space trajectory and the RF pulse
- Extension of the full Bloch simulation algorithm for  $k_T$ -points trajectory to spokes trajectory.



## 6 References

1. Nishimura D. Principles of Magnetic Resonance Imaging. Stanford University: Self Published; 1996.
2. Collins CM, Liu W, Schreiber W, Yang QX, Smith MB. Central brightening due to constructive interference with, without, and despite dielectric resonance. *Journal of magnetic resonance imaging* : JMRI 2005;21(2):192-196.
3. Vaughan JT, Garwood M, Collins CM, Liu W, DelaBarre L, Adriany G, Andersen P, Merkle H, Goebel R, Smith MB, Ugurbil K. 7T vs. 4T: RF power, homogeneity, and signal-to-noise comparison in head images. *Magnetic resonance in medicine : official journal of the Society of Magnetic Resonance in Medicine / Society of Magnetic Resonance in Medicine* 2001;46(1):24-30.
4. Katscher U, Bornert P. Parallel RF transmission in MRI. *NMR in biomedicine* 2006;19(3):393-400.
5. Wald LL, Adalsteinsson E. Parallel Transmit Technology for High Field MRI. *Magnetom FLASH* 2009.
6. Shellock FG, Crues JV. MR procedures: biologic effects, safety, and patient care. *Radiology* 2004;232(3):635-652.
7. Hennel F, Girard F, Loenneker T. "Silent" MRI with soft gradient pulses. *Magnetic resonance in medicine : official journal of the Society of Magnetic Resonance in Medicine / Society of Magnetic Resonance in Medicine* 1999;42(1):6-10.
8. McJury M, Shellock FG. Auditory noise associated with MR procedures: a review. *Journal of magnetic resonance imaging* : JMRI 2000;12(1):37-45.
9. Wald LL, Adalsteinsson E. Specific Absorption Rate (SAR) in Parallel Transmission (pTx). *Magnetom FLASH* 2010.
10. Guerin B, Gebhardt M, Cauley S, Adalsteinsson E, Wald LL. Local specific absorption rate (SAR), global SAR, transmitter power, and excitation accuracy trade-offs in low flip-angle parallel transmit pulse design. *Magnetic resonance in medicine : official journal of the Society of Magnetic Resonance in Medicine / Society of Magnetic Resonance in Medicine* 2013.
11. Collins CM, Wang Z, Smith MB. SAR assessment of transmit arrays: Deterministic calculation of worst- and best-case performance. in *Proceedings of the ISMRM* 2007:4803.
12. Cloos MA, Boulant N, Luong M, Ferrand G, Giacomini E, Hang MF, Wiggins CJ, Le Bihan D, Amadon A. Parallel-transmission-enabled magnetization-prepared rapid gradient-echo T1-weighted imaging of the human brain at 7 T. *NeuroImage* 2012;62(3):2140-2150.
13. Plewes DB, Kucharczyk W. Physics of MRI: a primer. *Journal of magnetic resonance imaging* : JMRI 2012;35(5):1038-1054.
14. Pauly J, Nishimura D, Macovski A. A k-space analysis of small-tip-angle excitation. 1989. *Journal of magnetic resonance* 2011;213(2):544-557.
15. Setsompop K, Wald LL, Alagappan V, Gagoski BA, Adalsteinsson E. Magnitude least squares optimization for parallel radio frequency excitation design demonstrated at 7 Tesla with eight channels. *Magnetic resonance in medicine : official journal of the Society of Magnetic Resonance in Medicine / Society of Magnetic Resonance in Medicine* 2008;59(4):908-915.
16. Eichfelder G, Gebhardt M. Local specific absorption rate control for parallel transmission by virtual observation points. *Magnetic resonance in medicine : official journal of the Society of*

- Magnetic Resonance in Medicine / Society of Magnetic Resonance in Medicine 2011;66(5):1468-1476.
17. Yip CY, Grissom WA, Fessler JA, Noll DC. Joint design of trajectory and RF pulses for parallel excitation. *Magnetic resonance in medicine : official journal of the Society of Magnetic Resonance in Medicine / Society of Magnetic Resonance in Medicine* 2007;58(3):598-604.
  18. Cloos MA, Boulant N, Luong M, Ferrand G, Giacomini E, Le Bihan D, Amadon A. kT -points: short three-dimensional tailored RF pulses for flip-angle homogenization over an extended volume. *Magnetic resonance in medicine : official journal of the Society of Magnetic Resonance in Medicine / Society of Magnetic Resonance in Medicine* 2012;67(1):72-80.
  19. Pauly J, Nishimura D, Macovski A. A Linear Class of Large-Tip-Angle Selective Excitation Pulses. *Journal of magnetic resonance imaging : JMRI* 1989;82:571-587.
  20. Pauly J, Le Roux P, Nishimura D, Macovski A. Parameter relations for the Shinnar-Le Roux selective excitation pulse design algorithm [NMR imaging]. *IEEE transactions on medical imaging* 1991;10(1):53-65.
  21. Setsompop K, Alagappan V, Zelinski AC, Potthast A, Fontius U, Hebrank F, Schmitt F, Wald LL, Adalsteinsson E. High-flip-angle slice-selective parallel RF transmission with 8 channels at 7 T. *Journal of magnetic resonance* 2008;195(1):76-84.
  22. Grissom WA, Yip CY, Wright SM, Fessler JA, Noll DC. Additive angle method for fast large-tip-angle RF pulse design in parallel excitation. *Magnetic resonance in medicine : official journal of the Society of Magnetic Resonance in Medicine / Society of Magnetic Resonance in Medicine* 2008;59(4):779-787.
  23. Xu D, King KF, Zhu Y, McKinnon GC, Liang ZP. Designing multichannel, multidimensional, arbitrary flip angle RF pulses using an optimal control approach. *Magnetic resonance in medicine : official journal of the Society of Magnetic Resonance in Medicine / Society of Magnetic Resonance in Medicine* 2008;59(3):547-560.
  24. Gumbrecht R. [MS]. Erlangen-Nurnberg: Friedrich-Alexander-Universitat 2010. 85 p.
  25. Bernstein MA, King KF, Zhou XJ. *Handbook of MRI Pulse Sequences*. London UK: Elsevier Inc.; 2004. 1017 p.
  26. Kozlov M, Turner R. Fast MRI coil analysis based on 3-D electromagnetic and RF circuit co-simulation. *Journal of magnetic resonance* 2009;200(1):147-152.
  27. Zaremba LA. Guidance for Industry and FDA Staff, Criteria for Significant Risk Investigations of Magnetic Resonance Diagnostic Devices. In: US Department of Health and Human Services FaDA, Center for Devices and Radiological Health, editor. Rockville, MD2003.